

A systematic study of earthquake detectability using Sentinel-1 Interferometric Wide-Swath data

Gareth J. Funning¹ and Astrid Garcia[†]

Department of Earth Sciences, University of California, Riverside, CA 92521, USA. E-mail: gareth@ucr.edu

Accepted 2018 October 12. Received 2018 October 4; in original form 2017 October 31

SUMMARY

The Sentinel-1 mission comprises two synthetic aperture radar satellites, each with a 12-d orbital repeat, orbiting 6 d apart within a narrow tube. The mission design promises the ability to respond quickly to earthquakes with InSAR, and to facilitate production of interferograms with good interferometric correlation globally. We report on our efforts to study global seismicity using Sentinel-1 Interferometric Wide-Swath data between April 2015 and December 2016. We select 35 potentially detectable terrestrial earthquakes in the range $5.5 \leq M_w \leq 7.8$ on the basis of their locations, depths and magnitudes, and process the first post-event interferogram with the shortest possible time span for each using the ISCE software. We evaluate each interferogram for earthquake deformation signals by visual inspection. We can identify deformation signals attributable to earthquakes in 18 of these interferograms (51 per cent); a further six interferograms (17 per cent) have ambiguous interferometric phase affected by tropospheric noise. 11 events (31 per cent) could not be identified from their interferograms. The majority of these failed detections were due to interferogram decorrelation, particularly apparent for earthquakes that occurred between 15°N and 15°S , where climate conditions promote dense vegetation. The majority of the ambiguous interferograms are affected by tropospheric noise, suggesting that techniques to mitigate such noise could improve detection performance. The largest event we do not detect with Sentinel-1 data is a $M_w 7.0$ earthquake that occurred in Vanuatu in April 2016; we also fail to detect the 2016 $M_w 6.2$ Kurayoshi earthquake in one out of two possible 24-d interferograms. We propose these as upper and lower estimates on the magnitude of completeness for earthquakes studied with Sentinel-1 data; to lower the magnitude of completeness we suggest that more frequent (e.g. 6-d) recurrence may be necessary in low latitude areas.

Key words: Radar interferometry; Satellite geodesy; Earthquake source observations.

1 INTRODUCTION

1.1 Studying earthquakes with InSAR

Since the 1992 Landers, California earthquake was detected by successfully interfering radar images acquired on repeat passes of the ERS-1 satellite (Massonnet *et al.* 1993), interferometric synthetic aperture radar (InSAR) has been a viable means of studying earthquakes with observations that are independent of seismology (see Massonnet & Feigl 1998; Bürgmann *et al.* 2000; Salvi *et al.* 2012; Elliott *et al.* 2016, for helpful reviews). With successive SAR satellite missions, our capabilities of detecting and studying earthquakes have improved as the capabilities of the satellites themselves have improved. We estimate, from a survey of the scientific literature,

that at the time of writing there are over 200 published studies of over 130 individual earthquakes using InSAR data as constraints on models of the earthquake source.

Using InSAR data to study earthquakes has several advantages over more traditional approaches. The line-of-sight displacement measurements made with InSAR provide more accurate measures of earthquake location than teleseismic methods (e.g. Weston *et al.* 2011, 2012), and give a similar level of location accuracy to local seismometer networks, but do not require expensive local infrastructure. These accurate locations can be used as ground truth for evaluations of different Earth velocity models (e.g. Ferreira *et al.* 2011), or for anchoring relative relocations of events to events of known location (e.g. Nissen *et al.* 2016). Even when not used directly on constraints on models of fault slip, interferograms of earthquakes (coseismic interferograms) can be directly of help to scientists undertaking field response. For example, phase discontinuities in coseismic interferograms of the 2003 Bam, Iran earthquake (Talebian

[†] Formerly at Riverside Community College.

et al. 2004), the 2010 El Mayor-Cucapah earthquake (Gonzalez-Garcia *et al.* 2010) and 2014 South Napa, California earthquake (DeLong *et al.* 2016) were all used to guide field geologists to surface ruptures that had been initially missed during the initial response to those events.

In recent years, a new generation of SAR satellite missions has been proposed or launched with the promise to boost our observational capability through reduced revisit times, more stable orbits and longer duty cycles (ability to acquire more data in each orbit). In this study, we examine in more detail one of these missions, the European Space Agency Sentinel-1 mission.

1.2 Factors that can impede earthquake detection with InSAR

While InSAR has improved our ability to measure the spatial patterns of deformation for many shallow earthquakes on or near land, it is not always successful. A principal limitation of InSAR is decorrelation, the reduction of InSAR signal quality, which can occur in certain surface or orbital conditions. Formally, decorrelation is the reduction of interferometric correlation, a measure of the coherence of the obtained interferometric phase. Interferometric correlation can be decomposed into several contributing components, including thermal noise, geometric effects, volumetric effects and temporal decorrelation (for detailed discussions, see the studies by Zebker & Villasenor 1992; Rosen *et al.* 2000; Fielding *et al.* 2005).

Of these components, thermal noise is typically neglected, given the high signal-to-noise ratios for modern SAR instruments in most settings (e.g. Weber Hoen & Zebker 2000; Wei & Sandwell 2010). Geometric effects on decorrelation are a result of differences of illumination angle caused by differences of orbital position, in turn causing changes in radar reflectivity within a radar pixel on the ground. This effect is particularly profound in areas of steep topographic slopes. Therefore, we would expect decreases in interferometric correlation with increasing perpendicular baselines. Volumetric effects on interferometric correlation relate to the expected scattering of radar from a volume of material; in most tectonic applications of InSAR, the most important such scatterer is vegetation. The C-band radars used in several major SAR satellites (e.g. the European Space Agency's ERS, Envisat and Sentinel-1 missions), are sensitive to objects with a length scale of 10 mm or larger (e.g. Fielding *et al.* 2005), which can include leaves, branches and trunks of trees, shrubs and other plants. We would therefore expect decreases in correlation in areas with dense vegetation. Finally, temporal decorrelation is the effect of changes and/or movements of the radar scatterers within a radar pixel. This can include changes to vegetation, such as growth, movement in the wind or the shedding of leaves, plus the effects of human activity, mass movements, flooding and/or earthquake-related damage to the surface or structures. The probability of such changes increases monotonically with time, such that decreases in correlation would be expected with increase in the time span of interferograms. We would also expect larger decreases in correlation due to temporal changes in more heavily vegetated areas.

A second factor that can impede earthquake detection with InSAR is noise from the atmosphere. There are two principal atmospheric noise sources in InSAR data—the presence of charged particles in the ionosphere, that can cause wavelength-dependent refraction of microwave radiation as it passes through, and the presence of water vapour in the troposphere that can introduce a

wavelength-independent delay to the propagating microwaves. Typically it is the longer wavelength radars (e.g. the L-band radars used by the ALOS and ALOS-2 satellites) that are most affected by ionospheric distortions, and we will neglect them in this study which focuses on results from shorter, C-band radars; in addition, advances in split-band SAR processing (e.g. Gomba *et al.* 2016) promise a means of correcting for these distortions in future. In contrast, tropospheric noise remains a significant issue with all satellite InSAR, especially when measuring small deformation signals (e.g. of a few centimetres), as the delay imparted to the propagating radar can be of the order of or larger than the signal of interest, and have a similar spatial length scale (kilometres to tens of kilometres). Although methods have been proposed to mitigate tropospheric noise, such as using GPS-estimated zenith delays (e.g. Li *et al.* 2006), optical imagery (e.g. Li *et al.* 2012), high resolution meteorological reanalysis data (e.g. Jolivet *et al.* 2011), there are operational issues that can prevent these solutions being universally applicable or useful—most notably limited data availability (e.g. in the case of GPS and optical imagery), lack of resolution (e.g. in the case of meteorological data), and lack of availability in real time. In this study, we do not apply atmospheric corrections routinely; instead, we assess the impact of atmospheric noise on our ability to detect earthquakes.

1.3 The Sentinel-1 mission

The Sentinel-1 satellite mission currently comprises two satellites (Sentinel-1A, launched 2014 April 3 and Sentinel-1B, launched 2016 April 22) in the same sun-synchronous polar orbit with a 12-d repeat, orbiting 6 d apart. The two satellites are identical, each carrying sufficient consumables to sustain a 12-yr mission span, and each carrying the same instrumentation (see Torres *et al.* 2012, for details). The satellites are navigated within a narrow orbital 'tube' (of the order of 200 m in diameter) to minimize the effects of variable viewing geometry on interferometry. A feature of the C-band (55.5 mm wavelength) SAR antennas on the Sentinel-1 satellites is their ability to acquire wide-swath data using Terrain Observation by Progressive Scans (TOPS; De Zan. & Guarnieri 2006) mode. Here, the radar beam sweeps backwards and forwards, with a squint angle that varies by $\pm 0.7^\circ$, in the direction of travel in a series of 'bursts', and also is switched sequentially from burst to burst between different subswaths each with a different incidence angle. The main benefit of TOPS mode is to allow the collection of radiometrically uniform wide-swath SAR data, absent the scalloping and variable signal-to-noise ratios in the azimuth direction that can result from other modes of wide-swath SAR, such as ScanSAR (e.g. Moore *et al.* 1981). In addition, a collateral benefit of TOPS mode acquisitions is that the overlap between successive bursts in each subswath enables the precise measurement of displacements in the azimuth direction in the overlap zones (e.g. Grandin *et al.* 2016).

The main TOPS mode used by the Sentinel-1 satellites, known as Interferometric Wide-Swath, or IW mode, has three subswaths that between them cover a swath of 250 km on the ground, with a range of incidence angles between 30° and 45° . The size of an individual pixel in IW mode is approximately 20 m in azimuth versus 5 m in range, degraded from the 5 m by 5 m pixel size that can be achieved if the instrument is operated in stripmap mode, as it was in select areas during the first year of operation of Sentinel-1A (e.g. Floyd *et al.* 2016). Since April 2015, however, IW mode has been the primary data acquisition mode over most of the Earth's land surface.

The mission to date has seen a gradual increase in revisit frequency over most land areas over time. During the initial phase of IW acquisitions, with only Sentinel-1A in orbit, and operational restrictions due to power and downlink capacity constraints, most areas of high tectonic strain rate were covered every 24 d in both ascending and descending orbits, 12-d repeat coverage being restricted to a few priority regions, such as continental Europe. With the launch and subsequent calibration/evaluation of Sentinel-1B completed in September 2016, along with improvements in downlink capacity, including the use of ERDS-A (European Data Relay System-A), revisit frequency is approaching 12 d in both ascending and descending modes over most land areas and 6 d in priority areas, such as Europe (Rosich *et al.* 2017).

1.4 Towards operational monitoring of earthquakes using Sentinel-1 data

The short revisit times of the Sentinel-1 satellites, along with the free and near-real time availability of the SLC data they produce, raise the possibility of the routine measurement of the crustal deformation due to shallow continental earthquakes globally. Not only would the short revisit times facilitate timely response to events, they should also minimize the effects of temporal decorrelation (e.g. due to vegetation or surface change); the tight orbital navigation should similarly minimize the effects of geometric decorrelation in areas of steep relief. Therefore, the expectation is that it should be possible to form successful interferometric pairs with the first post-event acquisition(s). These measurements could then be incorporated into the scientific and civil response to earthquakes (e.g. Salvi *et al.* 2012).

In this study, we aim to evaluate these expectations in other words, to assess the viability of the Sentinel-1 mission, and IW data in particular, as a tool for the operational monitoring of shallow earthquakes that occur on land. We systematically process Sentinel-1 IW interferograms for a trial set of events in order to assess the detectability of earthquakes under quasi-operational conditions—that is with a single, short time span interferogram produced with data acquired shortly after the event. We will show that event latitude is a stronger predictor of earthquake detectability using Sentinel-1 data than other criteria previously used, such as perpendicular baseline or interferogram minimum time span, a finding that has implications for mission operations in low-latitude regions.

2 PRODUCING INTERFEROGRAMS FOR POTENTIALLY DETECTABLE EARTHQUAKES

2.1 Depth and magnitude criteria for potentially detectable earthquakes

Compilations of earthquake models derived from InSAR data show that events of $M_w 5.5$ and larger are often detected by the technique (e.g. Funning 2005; Weston *et al.* 2011, 2012). In certain circumstances, smaller events have been identified, although not consistently. Lohman & Simons (2005) in a survey of 110 ERS interferograms of the Zagros mountains in Iran, identified five earthquakes in the magnitude range $4.7 \leq M_w \leq 5.4$ from 96 potential target events with $M_w > 4.5$. All of the detected events had centroid depths shallower than 5 km. Indeed, the depth of an earthquake is an important control on whether it can produce sufficient deformation to be detectable. Deeper earthquake sources will produce less

surface deformation than shallower events of the same size, and are thus less likely to be detectable (e.g. Mellors *et al.* 2004).

For this study, therefore, we propose to select events using paired magnitude and depth criteria, with shallower maximum hypocentral depths for smaller magnitude events. Guided by our past experience and the published literature (e.g. Mellors *et al.* 2004; Weston *et al.* 2011, 2012), we establish trial selection criteria: events with magnitudes in the range $5.5 \leq M_w < 6.0$ with hypocentral depths of 10 km or less, events in the range $6.0 \leq M_w < 7.0$ with hypocentral depths of 20 km or less, and events with $M_w \geq 7.0$ with hypocentral depths of 25 km or less.

In order to test the feasibility of detecting such events, we forward model the expected deformation associated with the least detectable events in each magnitude range—that is the deepest and smallest. For example, in the lowest magnitude range, a $M_w 5.5$ event with a hypocentre at 10 km would be the least detectable combination of size and depth. To estimate the source parameters for such model events, we make several simplifying assumptions. First, we assume that faults are equidimensional, with downdip width, W , equal to fault length, L . Second, we assume that average fault slip, u , is proportional to fault length (e.g. Scholz 2002). Third, the hypocentral depth for the earthquake is used as an estimate of the depth to the bottom edge of the fault plane, which is supported by detailed comparisons of InSAR source models and earthquake hypocentres (Weston *et al.* 2011). Therefore the base of each model fault is fixed to the maximum hypocentral depth used for each magnitude range.

By applying the first two assumptions, we can state the relationship between fault length and seismic moment, M_0 :

$$M_0 = \mu L W u = \mu k L^3, \quad (1)$$

where $k = u/L$ is a fixed slip-to-length ratio, and μ is the rigidity modulus. If k and M_0 are known, then we can rearrange the equation to obtain L :

$$L = \sqrt[3]{\frac{M_0}{\mu k}}. \quad (2)$$

Scholz (2002) highlighted that the slip-to-length ratio k varies as a function of tectonic setting, varying from 1.5×10^{-5} for interplate earthquakes, to 6.5×10^{-5} for events in intraplate settings. As a result, fault dimensions for a given moment/magnitude will also vary with setting—for example for a $M_w 5.5$ event ($M_0 = 2.1 \times 10^{17}$ Nm), an intraplate earthquake will have $L = 7.8$ km and $u = 12$ cm, versus 4.8 km and 31 cm for an interplate earthquake.

We use the fault dimensions and slip values estimated this way to produce forward-modeled interferograms for earthquakes in both interplate and intraplate settings, assuming square dislocations in an isotropic elastic half space (Okada 1985), and a fixed line-of-sight vector corresponding to the central subswath of a descending track Sentinel-1 IW scene (subswath 2; incidence angle 39.3°). We test both dip-slip and strike-slip fault models; the former with a dip of 45° and pure reverse slip, the latter with a vertical dip and pure right-lateral slip. We also test both E–W- and N–S-striking fault geometries, to see if the lack of sensitivity of satellite InSAR to north–south displacements (e.g. Funning *et al.* 2005) affects detectability. We plot these forward deformation models in Fig. 2.

We find that in all cases that we test, the peak-to-trough (i.e. maximum negative to maximum positive) LOS displacement is greater than 1 cm. In general we find that fault orientation does not impart a significant difference to the amplitude of the expected displacement, that dip-slip faults generate larger earthquake displacements than strike-slip faults, and that interplate earthquakes generate 50 per cent larger strike-slip displacements than intraplate

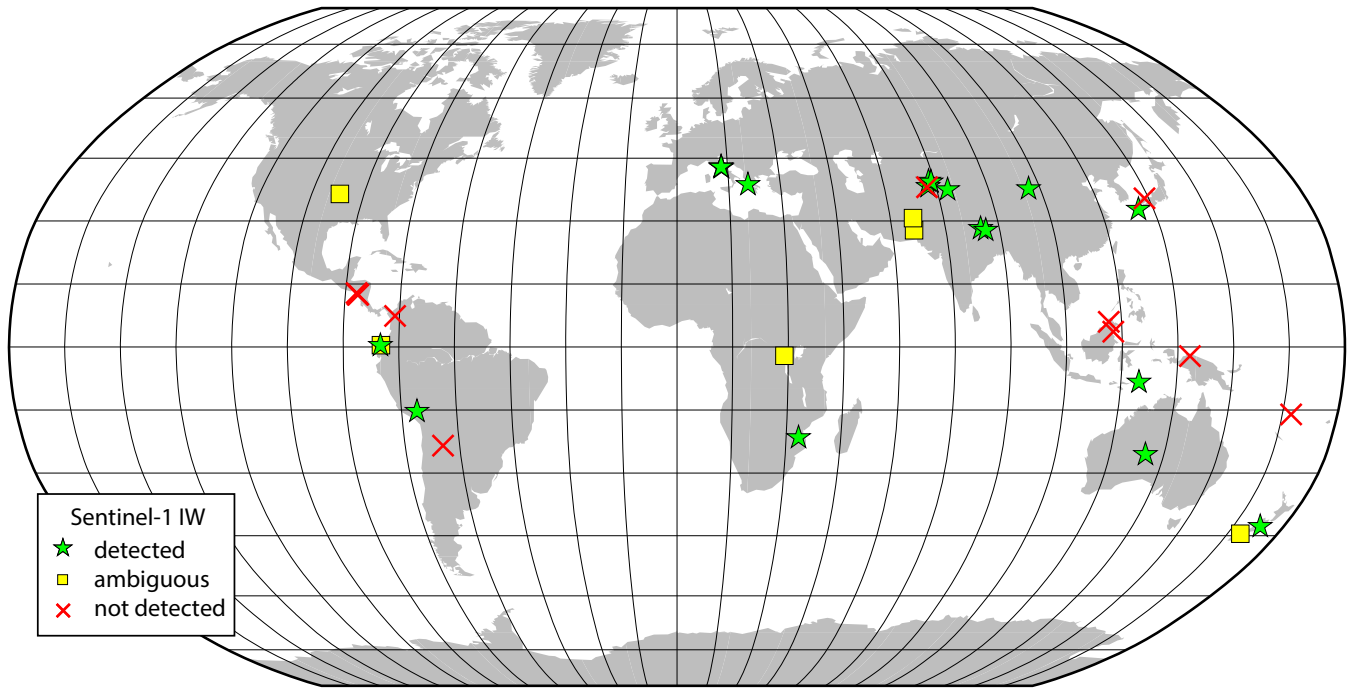


Figure 1. Map of the events for which Sentinel-1 interferograms were processed in this study. Green stars indicate that the event was detected from their interferograms; yellow squares represent ambiguous interferograms in which there is good interferometric correlation, but it is not clear which feature in the data is the earthquake; and red crosses indicate events that were not detected from their interferograms due to decorrelation.

events, due to the greater size of the rupturing fault patch meaning that the upper edge of the fault is closer to the surface. All of the strike-slip models show antisymmetric, lobate displacement patterns with paired positive and negative displacement lobes that are approximately equal in magnitude; the dip-slip event models have asymmetric deformation patterns, dominated by a single enclosed elliptical deformation feature, which in the case of the reverse fault tested here, is negative in sign, consistent with uplift. (The sense of deformation would become positive if a normal faulting mechanism were tested, with a similar amplitude.)

We suggest that in perfect conditions (i.e. in the absence of tropospheric noise and temporal decorrelation), all of these potential events should be detectable. We realize, however, that these conditions do not often arise, given the variability of troposphere conditions in particular, and that this is not the fault of the sensor; as we describe below, in such cases, we describe an interferogram where attempts at event detection in an area affected by tropospheric noise are unsuccessful as ‘ambiguous’, rather than failure (a ‘not detected’ case). In some recent cases, time-series processing has been used to separate coseismic displacements from spatially correlated noise for moderate-sized events (e.g. Fielding *et al.* 2017; Grandin *et al.* 2017), suggesting that such strategies could be used to extract a coseismic deformation signal from these ambiguous interferograms in future.

2.2 Event selection

Using the magnitude/depth criteria established above, we select a trial set of events for testing. We use the USGS global earthquake catalogue (earthquake.usgs.gov) to identify $M_w \geq 5.5$ earthquakes with epicentres located on land—either continents or islands—that occurred globally between 2015 April 1 and 2016 December 1. This time span approximately corresponds to the first 18 months

of global Sentinel-1 IW mode acquisitions, although we note that IW data were acquired in some regions prior to this. Finally, we exclude foreshocks and aftershocks that would appear in interferograms along with, and likely be masked by, the deformation of the corresponding mainshocks.

In total, we select 35 events (Fig. 1; Table 1). These are distributed across all continents, within the low- and mid-latitudes, and span a magnitude range between $M_w 5.5$ and $M_w 7.8$.

2.3 Data selection

For each event, we select pairs of Sentinel-1 IW scenes for the track/frame combination that has (i) the shortest repeat interval, (ii) the earliest post-event acquisition date and (iii) provides sufficient areal coverage around the USGS location so as to capture the full earthquake signal. These criteria are intended to minimize the effects of temporal decorrelation and inaccurate seismic catalogue locations, respectively. Where necessary, we select additional frames along track to guarantee coverage for a larger area around the seismic location. We do not prioritize particular viewing geometries (e.g. from ascending or descending tracks), or perpendicular baselines. The image combinations used in our analysis are listed in Table 1.

2.4 Data processing

We process the selected pairs of wide-swath SLCs using the ISCE (InSAR Scientific Computing Environment) software developed by the Jet Propulsion Laboratory, Caltech and Stanford University (Rosen *et al.* 2011; Gurrola *et al.* 2016). We use version 2.0.0_20170403 of the software, made available through the Western North America InSAR Consortium (<http://winsar.unavco.org/isce.h>

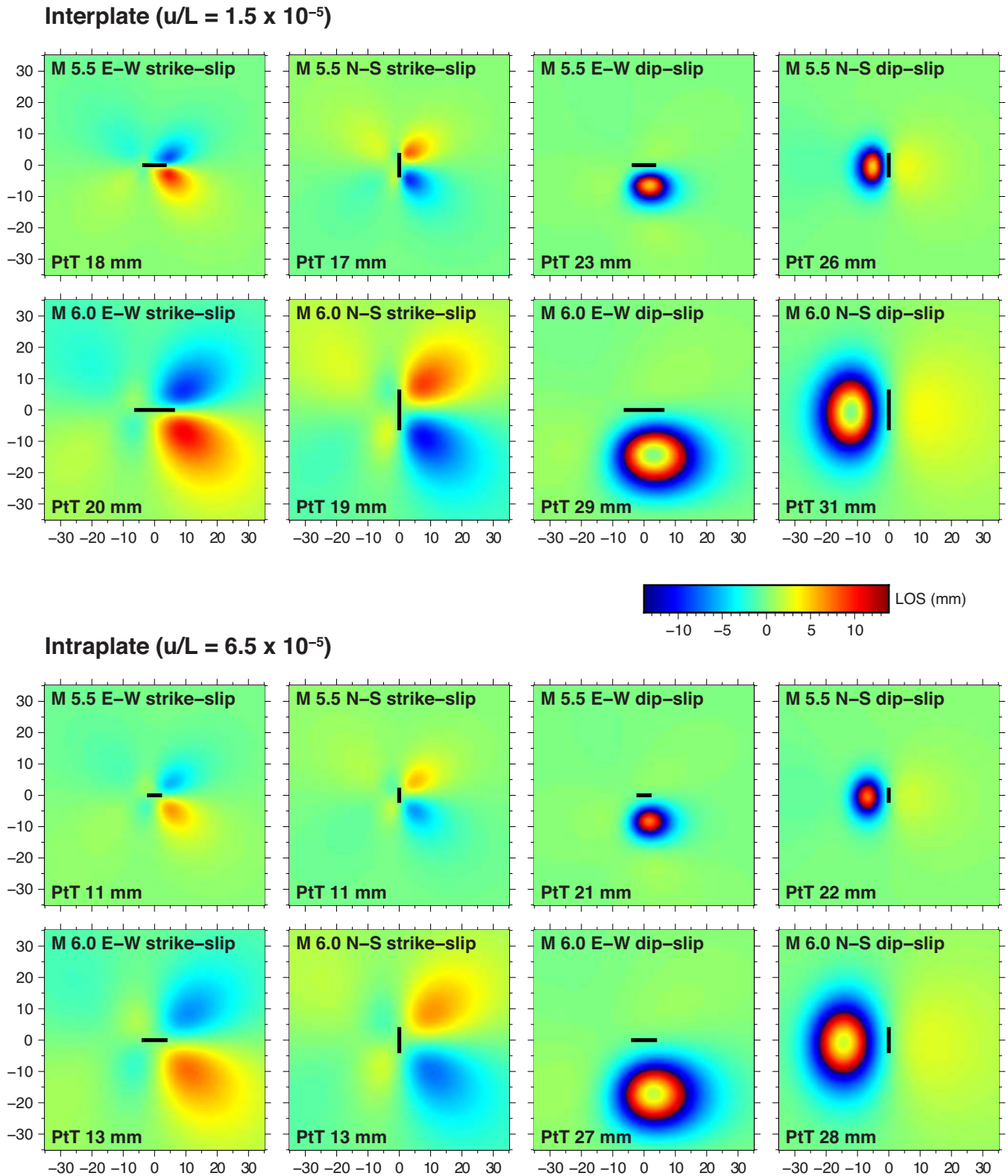


Figure 2. Expected earthquake deformation signals for marginally detectable earthquakes. Shown are forward-modeled line-of-sight displacements for earthquakes of minimum magnitude and maximum hypocentral depth within each magnitude/depth range considered (i.e. $M5.5$ at 10 km depth and $M6.0$ at 20 km depth). Both E–W- and N–S-striking faults and vertical strike-slip and 45° -dipping dip-slip geometries are tested, for two different slip-to-length ratios, corresponding to interplate earthquakes (top panel) and intraplate earthquakes (bottom panel), respectively. All models produce more than 1 cm of peak-to-trough (PtT) deformation; interplate earthquakes produce more deformation than intraplate events, particularly for strike-slip faults. Further details are given in the main text. [Solid black lines: surface projection of the modeled fault. Distances in km.]

Table 1. Details of Sentinel-1 Interferometric Wide-Swath coseismic interferograms processed in this study.

| Event date | Location | Country | M_w^a | Long. a | Lat. a | Depth a | Track | Geom. b | Swath | Date 1 | Date 2 | Δt^c | B_{\perp}^d | Corr. e | Detected? |
|------------|-------------------|-------------|---------|------------|-----------|------------|-------|------------|-------|------------|------------|--------------|---------------|------------|-----------|
| 2015/04/25 | Gorkha | Nepal | 7.8 | 84.731 | 28.230 | 8.2 | 019 | dsc | 1-3 | 2015/04/17 | 2015/04/29 | 12 | -39 | 0.35 | yes |
| 2015/05/04 | Wanaka | New Zealand | 5.6 | 168.883 | -44.523 | 10.0 | 096 | asc | 3 | 2015/04/10 | 2015/05/04 | 24 | 230 | 0.41 | ambig. |
| 2015/05/12 | Kodari | Nepal | 7.3 | 86.066 | 27.809 | 15.0 | 085 | asc | 2-3 | 2015/05/03 | 2015/05/15 | 12 | -89 | 0.37 | yes |
| 2015/06/04 | Ranau | Malaysia | 6.0 | 116.541 | 5.987 | 10.0 | 105 | dsc | 3 | 2015/05/16 | 2015/07/27 | 72 | -44 | 0.35 | no |
| 2015/07/03 | Pishan | China | 6.4 | 78.154 | 37.459 | 20.0 | 129 | asc | 2-3 | 2015/06/11 | 2015/07/05 | 24 | -39 | 0.52 | yes |
| 2015/08/07 | Lake Kivu | D. R. Congo | 5.5 | 28.951 | -2.091 | 10.0 | 174 | asc | 1 | 2015/08/01 | 2015/08/25 | 24 | 25 | 0.34 | ambig. |
| 2015/10/23 | Abepura | Indonesia | 5.8 | 138.267 | -2.166 | 8.0 | 155 | asc | 1-2 | 2015/10/11 | 2015/11/04 | 24 | 19 | 0.32 | no |
| 2015/11/04 | Alor | Indonesia | 6.5 | 124.875 | -8.338 | 20.0 | 039 | asc | 3 | 2015/10/15 | 2015/12/02 | 48 | 17 | 0.37 | yes |
| 2015/11/17 | Lefkada | Greece | 6.5 | 20.600 | 38.670 | 11.0 | 175 | asc | 1 | 2015/11/05 | 2015/11/17 | 12 | 28 | 0.60 | yes |
| 2015/11/29 | Yuto | Argentina | 5.5 | -64.586 | -23.478 | 10.0 | 003 | asc | 1 | 2015/10/12 | 2015/12/23 | 72 | -43 | 0.33 | no |
| 2015/12/07 | Murghob | Tajikistan | 7.2 | 72.780 | 38.211 | 22.0 | 005 | dsc | 1-2 | 2015/11/18 | 2015/12/12 | 24 | -139 | 0.38 | yes |
| 2015/12/20 | Tarakan | Indonesia | 6.1 | 117.636 | 3.646 | 14.6 | 105 | dsc | 1 | 2015/12/18 | 2016/01/11 | 24 | -40 | 0.33 | no |
| 2016/01/20 | Hongtu | China | 5.9 | 101.641 | 37.671 | 9.0 | 128 | asc | 2 | 2016/01/13 | 2016/02/06 | 24 | -17 | 0.57 | yes |
| 2016/03/18 | Vanj | Tajikistan | 5.6 | 72.411 | 38.023 | 10.0 | 100 | asc | 1 | 2016/03/11 | 2016/04/04 | 24 | 48 | 0.35 | no |
| 2016/03/21 | Khuzdar | Pakistan | 5.6 | 66.096 | 27.768 | 10.0 | 042 | dsc | 1-2 | 2016/03/03 | 2016/03/27 | 24 | -54 | 0.64 | ambig. |
| 2016/04/15 | Kumamoto | Japan | 7.0 | 130.754 | 32.791 | 10.0 | 156 | asc | 1-2 | 2016/04/08 | 2016/04/20 | 12 | -66 | 0.37 | yes |
| 2016/04/16 | Pedernales | Ecuador | 7.8 | -79.922 | 0.382 | 20.6 | 040 | dsc | 1-3 | 2016/04/12 | 2016/04/24 | 12 | 21 | 0.34 | yes |
| 2016/04/28 | Norsup | Vanuatu | 7.0 | 167.379 | -16.043 | 24.0 | 154 | asc | 3 | 2015/10/23 | 2016/10/23 | 366 | 23 | 0.35 | no |
| 2016/05/13 | Qila Abdullah | Pakistan | 5.5 | 66.388 | 30.659 | 10.0 | 151 | dsc | 2-3 | 2016/04/20 | 2016/05/14 | 24 | 49 | 0.54 | ambig. |
| 2016/05/18 | Muisne | Ecuador | 6.7 | -79.790 | 0.426 | 16.0 | 040 | dsc | 1-2 | 2016/05/06 | 2016/05/18 | 12 | 77 | 0.34 | ambig. |
| 2016/05/20 | Peternmann Ranges | Australia | 6.0 | 129.884 | -25.566 | 10.0 | 075 | dsc | 2-3 | 2015/10/17 | 2016/06/01 | 228 | 57 | 0.35 | yes |
| 2016/06/10 | Puerto Morazan | Nicaragua | 6.1 | -86.963 | 12.832 | 10.0 | 055 | dsc | 1-3 | 2016/05/19 | 2016/06/12 | 24 | -45 | 0.33 | no |
| 2016/06/26 | Sary-Tash | Kyrgyzstan | 6.4 | 73.339 | 39.479 | 13.6 | 100 | asc | 3 | 2016/06/15 | 2016/07/09 | 24 | 13 | 0.53 | yes |
| 2016/08/24 | Amatrice | Italy | 6.2 | 13.188 | 42.723 | 4.4 | 117 | asc | 3 | 2016/08/21 | 2016/08/27 | 6 | 28 | 0.49 | yes |
| 2016/09/03 | Pawnee | USA | 5.8 | -96.929 | 36.425 | 5.6 | 034 | asc | 2 | 2016/09/03 | 2016/09/09 | 6 | 149 | 0.42 | ambig. |
| 2016/09/14 | Mutata | Colombia | 6.0 | -76.169 | 7.374 | 18.0 | 142 | dsc | 1-3 | 2016/08/29 | 2016/09/22 | 24 | -86 | 0.34 | no |
| 2016/09/15 | La Paz Centro | Nicaragua | 5.7 | -86.642 | 12.440 | 10.0 | 055 | dsc | 1-2 | 2016/08/23 | 2016/09/16 | 24 | 50 | 0.32 | no |
| 2016/09/22 | Machaze | Mozambique | 5.6 | 33.411 | -21.552 | 10.0 | 174 | asc | 1 | 2016/09/12 | 2016/09/24 | 12 | 50 | 0.49 | yes |
| 2016/09/28 | Nagarote | Nicaragua | 5.5 | -86.515 | 12.442 | 7.6 | 055 | dsc | 1-2 | 2016/09/16 | 2016/10/04 | 18 | 52 | 0.32 | no |
| 2016/10/21 | Kurayoshi | Japan | 6.2 | 133.809 | 35.374 | 5.6 | 090 | dsc | 1-2 | 2016/09/30 | 2016/10/24 | 24 | 86 | 0.34 | no |
| 2016/10/26 | Visso | Italy | 6.1 | 13.067 | 42.956 | 10.0 | 044 | asc | 1 | 2016/10/21 | 2016/10/27 | 6 | -72 | 0.41 | yes |
| 2016/10/30 | Norcia | Italy | 6.6 | 13.096 | 42.862 | 8.0 | 044 | asc | 1-2 | 2016/10/27 | 2016/11/02 | 6 | -18 | 0.45 | yes |
| 2016/11/13 | Kaikoura | New Zealand | 7.8 | 173.054 | -42.737 | 22.0 | 052 | asc | 1-3 | 2016/11/03 | 2016/11/15 | 12 | 10 | 0.44 | yes |
| 2016/11/25 | Akto | China | 6.6 | 73.978 | 39.273 | 17.0 | 027 | asc | 1-2 | 2016/11/13 | 2016/12/07 | 24 | 99 | 0.42 | yes |
| 2016/12/01 | Huarichancara | Peru | 9.3 | -70.827 | -15.312 | 10.0 | 149 | asc | 1 | 2016/11/15 | 2016/12/09 | 24 | 18 | 0.54 | yes |

^aMagnitude and hypocentral location information taken from the USGS catalogue; depths in km. ^bInterferogram viewing geometry [asc: ascending; dsc: descending]. ^cInterferogram time span in days. ^dPerpendicular baseline (m). ^eMean epicentral correlation (see Section 3.2).

tml). All data are processed using the standard *topsApp.py* processing flow, which we describe briefly below. [It should be noted that while there has been significant convergence in the methods used by different InSAR processing packages over the last few years, different approaches to, for instance, image coregistration may have some impact on the processed output from different software, for example different levels of interferometric correlation.]

The first step is burst-by-burst registration of both SLC images to the digital elevation model (DEM; the Shuttle Radar Topography Mission 1 arcsecond product of Farr *et al.* 2007, is used here). This is followed by coarse registration of the DEM-registered SLC bursts to each other and preliminary interferogram generation in burst overlap regions. Next, enhanced spectral diversity (ESD) matching in burst overlap regions is employed to provide precise image alignment (to one thousandth of a pixel in azimuth), followed by a further refinement of the registration of the SLCs for each burst in range, and computation of interferograms for each burst. These burst interferograms are then merged into a single interferogram, filtered using a power spectrum filter (power-law exponent 0.5, window size 5×5 pixels; Goldstein & Werner 1998), and geocoded. Optionally, if it is subsequently determined that there is an earthquake signal in the interferogram, we can mask out low correlation areas and unwrap it using the snaphu algorithm (Chen & Zebker 2002) prior to geocoding.

This procedure can operate on a single subswath or for multiple subswaths, according to need; in the latter case, the bursts from the multiple subswaths are treated separately until the burst interferogram merging step. The selection of which subswaths to process is made initially based on the seismic catalogue location, and expanded to cover a ~ 50 km radius around the catalogue location based on need (i.e. if an earthquake is not initially detected). As a post-processing step, where necessary we also make use of the water mask estimation feature in ISCE to exclude areas that are decorrelated due to bodies of water at the surface.

3 IDENTIFICATION OF EARTHQUAKE SIGNALS

The determination of whether an individual earthquake is detected by InSAR is made by visual inspection of the wrapped, geocoded interferogram in the vicinity of the USGS catalogue location. Here we explain our classification scheme for earthquake detection, and also how we quantify interferogram decorrelation in the vicinity of the earthquake epicentre.

3.1 Classification of earthquake detection

We classify events as either detected, ambiguous or not detected, based upon their appearance, as we shall describe below:

Detected. A clear, unambiguous detection of an event typically requires a diagnostically lobate deformation pattern (e.g. Fig. 2), multiple deformation fringes and/or a high fringe gradient, in an interferogram that usually has low decorrelation in the area of interest. In the cases of the smaller detected earthquakes, there was generally also a low level of atmospheric noise in the area of interest.

Ambiguous. Events with this classification typically have low decorrelation but significant atmospheric noise that makes it difficult to identify the earthquake. The appearance of most of these interferograms was ‘blobby’—containing multiple areas with interferometric phase changes in the approximate area of interest, but it is not clear if any of them corresponds to the earthquake. We

also used this classification for a noisy interferogram that had some visible signal, that we could not definitively attribute to an earthquake (see Section 4.3 below). It may be that some of these events could ultimately be revealed by using interferogram differencing (e.g. Talebian *et al.* 2004), averaging (e.g. Fielding *et al.* 2004) or time-series analysis (e.g. Grandin *et al.* 2017; Fielding *et al.* 2017) to remove or mitigate the atmospheric noise.

Not detected. We reserve this classification for events whose coseismic interferograms show significant decorrelation in the area of interest, so that no part of the earthquake deformation signal can be confidently identified. In these ‘non-detection’ cases, even if the earthquake could have generated sufficient surface deformation to be observed (in optimal conditions), the interferogram would have been unable to resolve it. We note that in our event selection process, events that would be obscured by surface water were excluded from our analysis; thus decorrelation of the land surface is responsible for the lack of a detection in these cases.

In cases where the initial subswath processing does not reveal an earthquake (in ambiguous or not detected cases), where possible we reprocess the data to include a wider area (a minimum of 50 km) around its USGS earthquake catalogue location—by processing all additional subswaths—to ensure that the lack of detection was not due to a location error.

We show representative examples of interferograms of detected, ambiguous and not detected events in Fig. 3. We show additional coseismic interferograms as case study examples in Section 4. The remainder are provided as a set of supplementary figures (Figs S1–S35).

We find that we can identify deformation signals attributable to earthquakes in a little over half of the events tested (18 out of 35 events, 51 per cent). A further 17 per cent of events (6 out of 35) have ambiguous coseismic interferograms. 31 per cent of events (11 out of 35) could not be identified from their interferograms. The largest earthquakes in our trial set, the $M_w 7.8$ 2015 Gorkha, Nepal (Fig. S1), 2016 Pedernales, Ecuador (Fig. S17) and 2016 Kaikoura New Zealand (Fig. S33) events, were all successfully detected. The smallest event that was successfully detected was a $M_w 5.6$ event from Mozambique (Fig. S28).

The map pattern of successful and unsuccessful detections (Fig. 1) is strongly latitudinal. The latitudinal zone with the lowest percentage of detected events (and the highest percentage of events that were not detected) is a band between 15°S and 15°N . Here, there are only two confirmed detections, versus six non-detections. This is a zone that includes tropical rainforests in Central and South America, Africa and Southeast Asia, raising the possibility that decorrelation due to the dense vegetation in those areas is a major impediment to earthquake detection. The mid-latitude bands, between 15°S and 45°S (four events detected, two events not detected), and between 15°N and 45°N (12 events detected, two event not detected), in contrast, have a majority of successful detections. These latitude ranges, although they have forest vegetation in some areas, are more likely to include plains, high mountains and deserts, areas with low vegetation density, and thus are less likely to decorrelate. We will revisit these relationships between latitude (and implied vegetation density), interferometric correlation and detectability in more detail in Section 5.

An additional concern that we identify is that infrequent image coverage over some areas of interest are likely exacerbating problems with temporal decorrelation. Long revisit times increase the probability of changes occurring to radar scatterers on the ground, the underlying cause of temporal decorrelation. In several of our non-detection cases, the shortest interval between acquisitions was

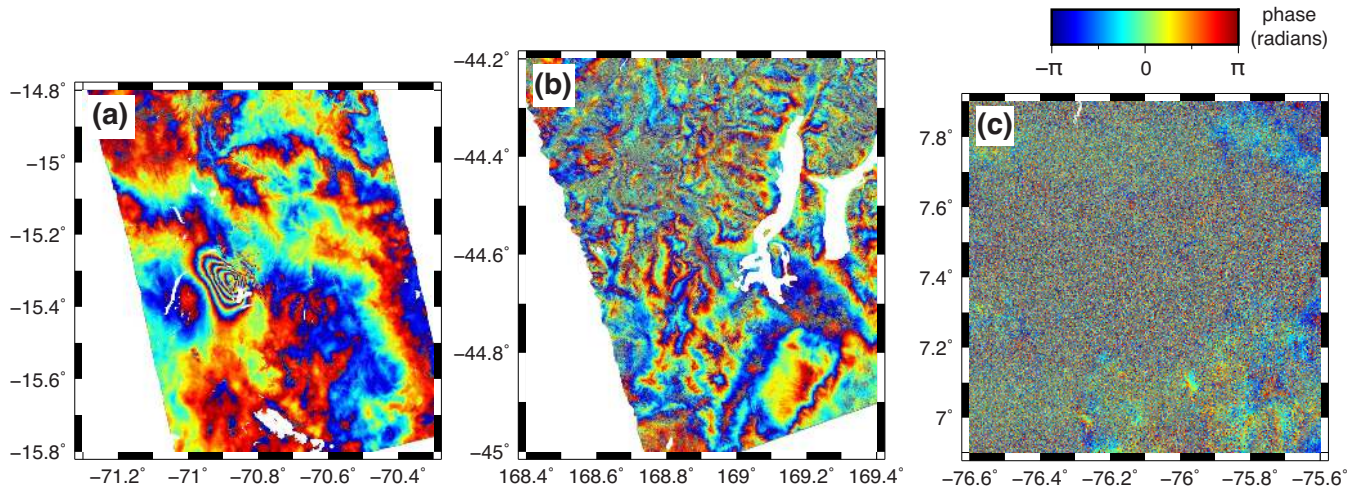


Figure 3. Examples of different categories of earthquake interferograms. (a) Interferogram showing a detected earthquake (Huarichancara, Peru, 2016 December 1, M_w 6.3). The clustered concentric fringes close to the centre of the image are consistent with the expected range increase for a normal-faulting earthquake. (b) Ambiguous interferogram—there is a reasonable level of interferometric correlation, but it is not clear whether any of the fringes represent an earthquake, rather than tropospheric noise (Wanaka, New Zealand, 2015 May 4, M_w 5.6). (c) Interferogram in which an earthquake was not detected, due to decorrelation (Mutata, Colombia, 2016 September 14, M_w 6.0). In each case, an area approximately centred on the USGS epicentre is shown. Details of the interferograms are given in Table 1.

of the order of 2 months or longer (e.g. Ranau, Malaysia, 2015, 72 d, Fig. S4; Yuto, Argentina, 2015, 72 d, Fig. S10), sufficient to cause extreme decorrelation in vegetated areas. With the launch of Sentinel-1B providing additional observational capacity, however, we find that 24 d is the maximum repeat interval for events from mid-2016 onwards.

3.2 Mean epicentral correlation

To quantify interferometric correlation with a view to estimating its influence on earthquake detectability, we suggest a scheme to estimate the average correlation in the vicinity of each earthquake epicentre. We use the definition of interferometric correlation used within both the ROI-PAC and ISCE processing suites—the averaged power of the interferometric product, normalized by the square root of the products of the averaged powers of the individual contributing SAR signals, over a specified local pixel window (e.g. Rosen *et al.* 2000). ISCE uses a 5×5 pixel window, applied to the coregistered SLCs to produce a correlation image, named ‘topophase.cor.geo’, that is not affected or altered by interferogram filtering.

We extract from these correlation images for each event, where possible, a square region 100 km in diameter centred on the USGS earthquake epicentre. In the cases where event epicentres are located within 50 km of the edge of the interferogram, the interferogram extent is used instead as a bound in that direction. We use the water mask produced using the ‘waterMask.py’ script in ISCE to mask out areas of known surface water, such as oceans, seas, rivers and lakes. From the remaining unmasked correlation data we calculate the mean of these correlation values, a quantity that we name the ‘mean epicentral correlation’ (MCE), for each event. We compile these values in Table 1.

In general, we find that MCE is effective at discriminating between sufficient levels of correlation ($MCE \geq 0.36$; zero non-detections due to decorrelation), and insufficient ($MCE < 0.34$; zero detected or ambiguous cases). In the transitional range $0.34 \leq MCE < 0.36$, corresponding to 10 of our interferograms, we find a mixture of detections (3), ambiguous cases (2) and non-detections

(5). Among these, most of the detected events are large earthquakes (i.e. two M_w 7.8 events—the Gorkha and Pedernales earthquakes), whereas most of the events that are not detected are at the smaller end of the magnitude range (four are in the range M_w 5.6–6.2), suggesting that larger earthquakes may be more detectable than smaller events in interferograms with marginal levels of correlation. We will explore these issues surrounding decorrelation in more detail in Section 5.

4 EARTHQUAKE DETECTION CASE STUDIES

Here we explore a few illustrative examples of earthquakes in greater detail.

4.1 The 2015 Alor, Indonesia earthquake

On 2015 November 4, a M_w 6.5 earthquake struck Alor Island (Pulau Alor), East Nusa Tenggara Province, Indonesia. The event, which occurred at 18:44 local time, damaged approximately 1500 homes and other buildings. No injuries were reported. Alor Island is located on the southern edge of the Banda Sea, a region dominated by N–S tectonic convergence driven by subduction to the north and south, primarily accommodated regionally by slip on the Wetar Thrust, a major backarc thrust structure located offshore to the north (McCaffrey, 1996). The USGS W-phase moment tensor for the event is consistent with right-lateral oblique-normal slip on an ESE-striking structure, suggesting that the fault responsible is involved in accommodating arc-parallel (and convergence-perpendicular) extension.

Despite occurring at least 7 months after the commencement of large-scale Sentinel-1 IW data acquisitions over major tectonic areas, data availability for the Alor earthquake is very poor. No descending track data was acquired over Alor Island prior to the earthquake. Also, although the island of Timor, located ~ 50 km to the southeast, is covered by frequent ascending track acquisitions, in all but a handful of cases, the data takes do not extend northward beyond the southern shore of Alor. We were only able to form

two ascending track interferograms that covered the catalogue location of the earthquake—an interferogram with a 48-d time span (track 039), and another with a 450-d time span (track 141). These interferograms are plotted in Fig. 4, with details given in Table 1.

Both Sentinel-1 interferograms are noisy, showing the effects of temporal decorrelation. As expected, the longer time span track 141 interferogram is the more severely affected of the two, with limited useable signal. However, despite the significant noise levels, both interferograms show features that can be interpreted as coseismic deformation. Most convincingly, the track 039 interferogram shows a series of five concentric fringes, with a steep E–W fringe gradient towards the eastern edge of the interferogram, suggesting that this part of the interferogram is close to the causative fault for the earthquake. With careful examination, some of these features can also be identified in the track 141 interferogram, which covers an area further to the east, suggesting that they are robust features of the coseismic deformation. In addition, another high fringe-gradient area can be identified further to the east, potentially another feature of the deformation pattern indicating proximity to the earthquake source, although given the high noise level it is difficult to learn too much about the details of the earthquake from it, except perhaps that the earthquake source should be located somewhere between the two high-fringe gradient areas.

To confirm that the features we identify are indeed related to the Alor earthquake, we process additional interferograms from the area, using descending track SAR data acquired by the ALOS-2 satellite and the ‘insarApp.py’ processing flow in the ISCE software. We would expect that the longer, L-band (23.6 cm wavelength) SAR on ALOS-2 should be much less susceptible to temporal decorrelation than the C-band instrument on Sentinel-1. This is indeed confirmed by the best of these interferograms (Fig. 4; Table 2) which shows an excellent level of interferometric correlation and a clear earthquake deformation signal, with seven concentric fringes (corresponding to ~ 70 cm of line-of-sight displacement) to the southwest of a phase discontinuity (the likely location of the fault), and three fringes to the northeast. The large area of concentric fringes seen in both Sentinel-1 interferograms is located somewhat to the west of the southwestern fringes in the ALOS-2 data, likely reflecting the greater sensitivity of the Sentinel-1 satellites to crustal deformation (four Sentinel-1 fringes being roughly equivalent to one ALOS-2 fringe, in terms of line-of-sight displacement), and also the different viewing geometries of the two sets of interferograms, with the Sentinel-1 data coming from ascending tracks and the ALOS-2 data from a descending track, meaning that the significant expected E–W deformation in the earthquake would be recorded differently in each.

4.2 The 2016 Kurayoshi, Japan earthquake

The $M_w 6.2$ Kurayoshi earthquake struck Tottori Prefecture (western Honshu), Japan on 2016 October 21 at 14:07 local time. Although the event caused no fatalities, there were five reported injuries in Tottori Prefecture, 2700 local residents were rendered temporarily homeless, and over 77 000 households and businesses in the region were affected by power outages. The USGS W-phase moment tensor for the event supports left-lateral strike-slip on a subvertical NNW-striking fault, consistent with the tectonic deformation style in western Honshu, where Quaternary faulting and earthquake moment tensors indicate that tectonic convergence is accommodated by conjugate strike-slip faulting (e.g. Wesnousky *et al.* 1982).

The earthquake occurred in a region of Japan where there was regular acquisition of SAR data on both ascending and descending tracks every 24 d, and thus the event is covered by two 24-d coseismic SAR image pairs (Fig. 5). We initially processed the descending track interferogram (Sentinel-1 track 090), which had the earlier post-event image of the two possibilities (24 October, versus 5 November for the ascending track; full details given in Table 2). There is no clear indication of an earthquake in this interferogram, which we show in Fig. 5(a), suggesting that this event should be classified as a non-detection. In particular, there is significant decorrelation in the vicinity of the USGS catalogue location for the event, which obscures any characteristic deformation that may have occurred there. Indeed, reports from the initial earthquake response in Japan, showing both significant coseismic GPS displacements and clear deformation signals in interferograms from the ALOS-2 satellite (see <http://www.gsi.go.jp/cais/topic161027-index-e.html> for more details) in the same area covered by our interferogram, suggest that coseismic deformation ought to be detectable with Sentinel-1, if decorrelation were low.

In contrast, the ascending track (track 083) Sentinel-1 interferogram, shown in Fig. 5(b), shows a very different picture of the earthquake. In this case, decorrelation is lower, and a clear four-quadrant deformation pattern, consistent with strike-slip deformation on a N–S oriented fault, can be identified.

The cause for this striking difference in decorrelation between the two image pairs could potentially be related to the perpendicular baselines between their imaging positions. While the two pairs both have the same time span—24 d—and thus would be expected to have similar levels of temporal decorrelation, larger perpendicular baselines could result in more significant levels of geometric decorrelation, particularly in areas of rugged terrain. The lower-decorrelation ascending track interferogram indeed has a shorter perpendicular baseline (30 m) than the higher-decorrelation descending track (86 m) suggesting that geometric decorrelation is a viable explanation for the difference between the two interferograms.

4.3 The 2016 Muisne, Ecuador earthquake

The $M_w 6.7$ 2016 May 18 Muisne, Ecuador earthquake was an aftershock of a larger event, the $M_w 7.8$ Pedernales earthquake (2016 April 16; Fig. S17). The event, located by the USGS 33 km southeast of the city of Muisne at an estimated depth of 16 km and striking in early hours of the morning, local time, reportedly caused one fatality and 85 injuries and disrupted classes at schools in Esmeraldas and Manabi provinces. It was followed nine hours later by a second, larger event ($M_w 6.9$), with an epicentre approximately 20 km to the ENE and greater estimated depth of 30 km; no additional casualties were reported. Only the earlier and shallower of the two events fulfils our event selection criteria and was thus targeted for study with InSAR.

Following the Pedernales earthquake, 12-d repeat acquisitions were made over the northwest coast of Ecuador in both descending and ascending geometries. We process each of the 12-d coseismic pairs; both the descending (track 040) and ascending (track 018) interferograms are plotted in Fig. 6 (details given in Tables 1 and 2). The epicentral region of the Muisne and Pedernales earthquakes is dominated by tropical rainforest vegetation, and thus issues with decorrelation are expected. We find that the interferograms are decorrelated to a level that is close to the limit of usability, and cannot identify unambiguously a signal that we can attribute to

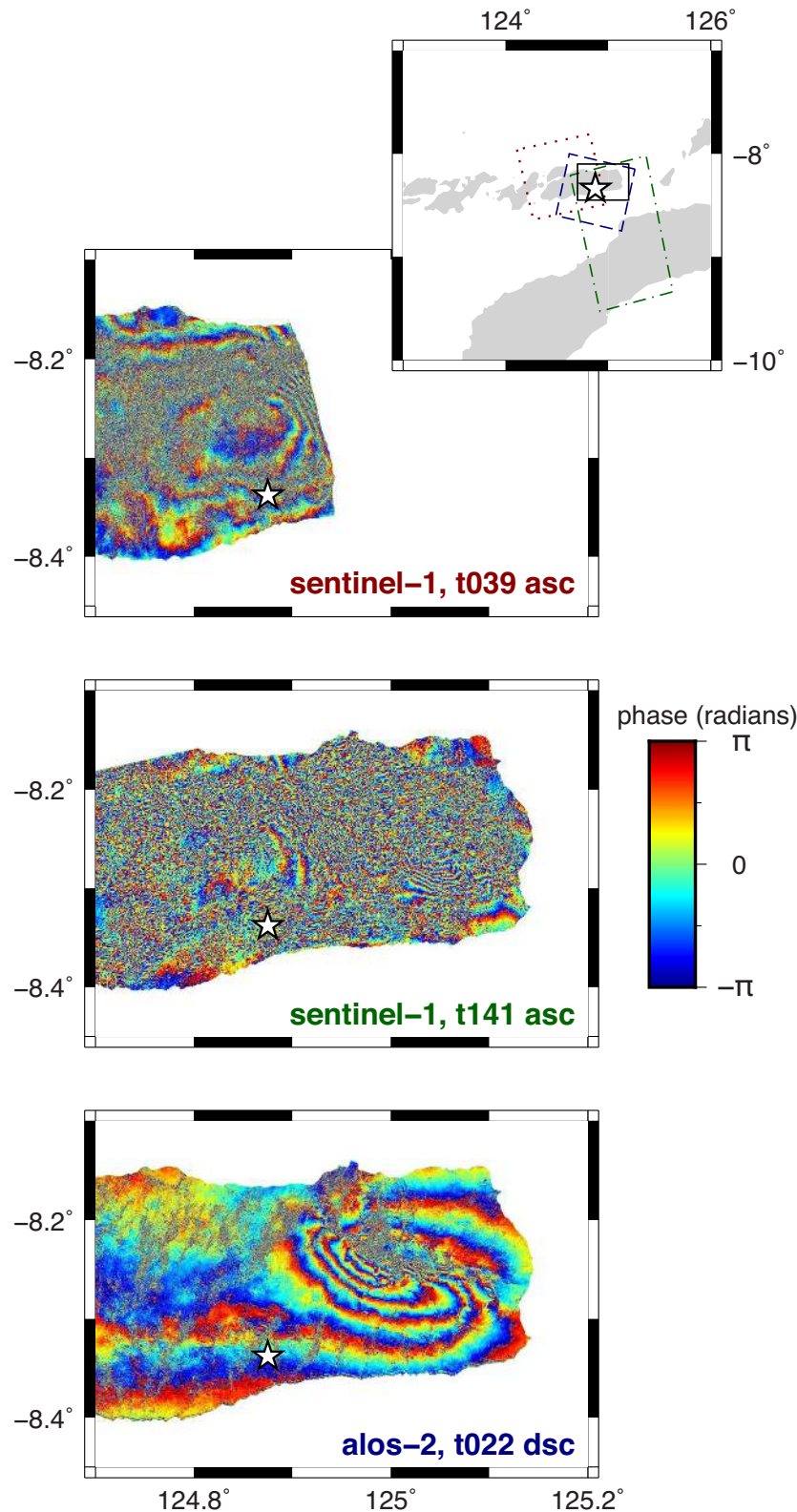


Figure 4. Interferograms of the 2015 Alor, Indonesia earthquake. Top panel: The shortest time span Sentinel-1 interferogram (48 d), from ascending track 039. Concentric fringes located north of the USGS epicentre for this event (white star), as well as the high fringe gradient at the eastern edge of the interferogram are features of the coseismic deformation. Middle panel: Longer time span Sentinel-1 interferogram (450 d) from the neighbouring ascending track (track 141). Some of the same features can be identified, although the amount of decorrelation is significantly worse. Bottom panel: ALOS-2 stripmap interferogram (track 022, descending) showing peak surface deformation at the location of the high fringe gradient in the top panel. The improved interferometric correlation in this interferogram reflects the longer, L-band, radar wavelength of the ALOS-2 satellite. Inset shows locations of the different interferogram frames. [Red dots: Sentinel-1 track 039; green dot-dashes: Sentinel-1 track 141; blue dashes: ALOS-2 track 022.].

Table 2. Details of supplemental coseismic interferograms processed in this study.

| Event date | Location | Mission | Track | Geom. ^a | Swath | Date 1 | Date 2 | Δt ^b | B_{\perp} ^c |
|------------|-----------|------------|-------|--------------------|----------|------------|------------|-------------------------|--------------------------|
| 2015/11/04 | Alor | Sentinel-1 | 141 | asc | 1 | 2015/09/04 | 2016/12/27 | 450 | −20 |
| 2015/11/04 | Alor | ALOS-2 | 022 | dsc | SM3 | 2015/03/04 | 2016/03/02 | 364 | −20 |
| 2016/04/28 | Norsup | ALOS-2 | 101 | asc | WD1, 2–4 | 2016/02/20 | 2016/07/23 | 154 | 141 |
| 2016/05/18 | Muisne | Sentinel-1 | 018 | asc | 1–3 | 2016/05/16 | 2016/05/28 | 12 | 9 |
| 2016/10/21 | Kurayoshi | Sentinel-1 | 083 | asc | 2–3 | 2016/10/12 | 2016/11/05 | 24 | 30 |

^aInterferogram viewing geometry [asc: ascending; dsc: descending]. ^bInterferogram time span in days. ^cPerpendicular baseline (m).

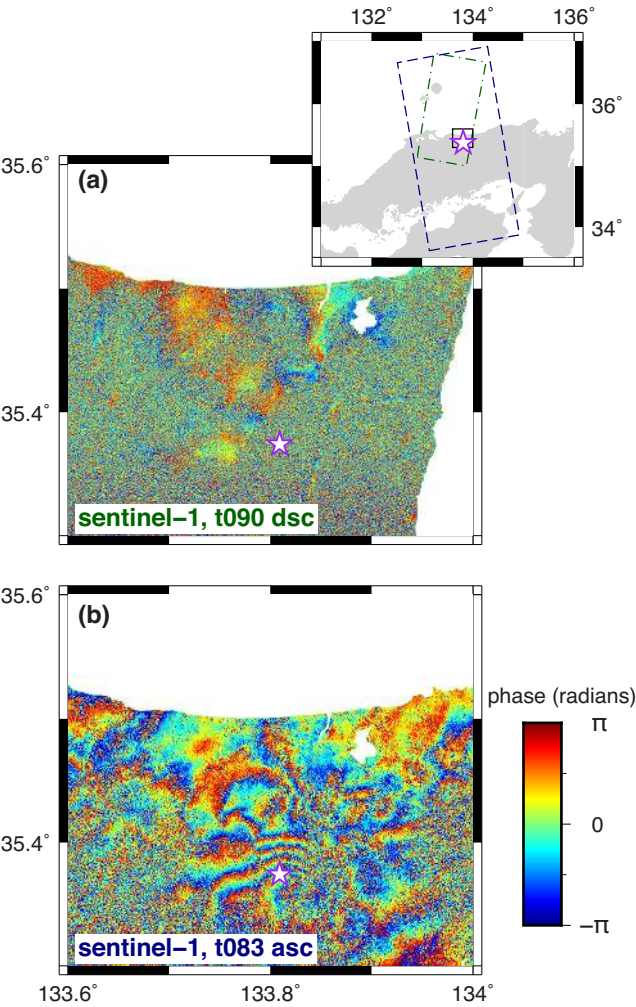


Figure 5. Comparison of two Sentinel-1 interferograms spanning the 2016 Kurayoshi, Japan earthquake, in the vicinity of the USGS epicentre (white star). (a) The first post-event interferogram (24-d time span, post-event acquisition date 2016/10/24), from descending track 090. This is a non-detection; there is insufficient detail in the correlated areas of the interferogram to identify an earthquake. (b) A later interferogram (24-d time span, post-event acquisition date 2016/11/05), from ascending track 083. This interferogram has sufficiently high correlation that deformation fringes from the earthquake can be identified. Inset shows locations of the different interferogram frames. [Green dot–dashes: Sentinel-1 track 090; blue dashes: Sentinel-1 track 083.].

an earthquake. In addition, both interferograms contain far-field fringes that could be attributed to tropospheric water vapour, that additionally impair our ability to identify deformation features.

The descending track interferogram (Fig. 6a), which was the first interferogram that could be formed after the event (post-event acquisition ~16 hr after the earthquake) shows a pair of concentric

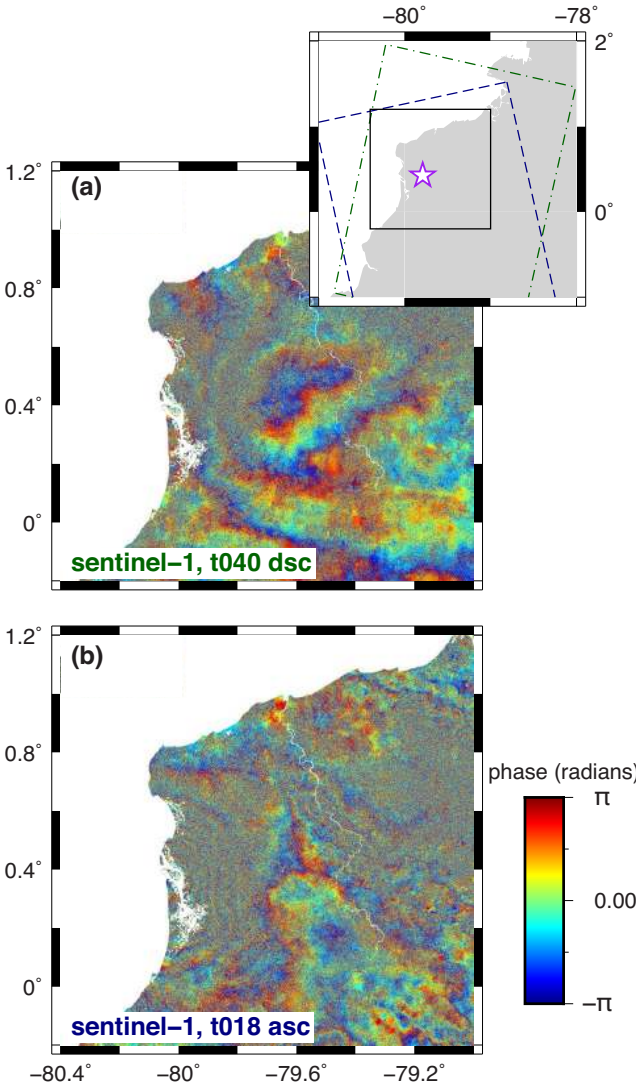


Figure 6. Sentinel-1 interferograms spanning the 2016 Muisne, Ecuador earthquake. (a) The first post-event interferogram (12-d time span, post-event acquisition date 2016 May 18), from descending track 040. This is an ambiguous interferogram—although correlation is low, there are fringes present, although it is not clear that they represent an earthquake. (b) A later interferogram (24-d time span, post-event acquisition date 2016 May 28), from ascending track 018. In this case, despite the low level of correlation, ~6 concentric fringes can be identified close to the shore. Inset shows location of interferogram frames. [Green dot–dashes: track 040; blue dashes: track 018; white star: USGS epicentre.].

fringes, covering an area approximately 60 km wide, to the east of the USGS epicentre. These fringes may represent deformation, but could also be interpreted as the result of long-wavelength tropospheric noise. On the basis of this interferogram, we classify the event as ambiguous – we have reasonable doubt that the earthquake is represented in the first post-event data. If the fringes represent deformation, they would be equivalent to ~ 6 cm of range increase, consistent with subsidence and/or westward displacement.

There is no equivalent signal in the ascending track interferogram (Fig. 6b; post-event acquisition 10 d after the earthquake) in this area, suggesting that the feature identified in the descending track interferogram is not a purely vertical signal. Instead, we identify approximately six concentric fringes, centred approximately 30 km to the west of the USGS epicentre, close to the coast between 0.1°N and 0.7°N , indicating approximately 17 cm of displacement with a sense of motion (range decrease) consistent with uplift and/or westward motion. These fringes overlap completely with the deformation field of the Pedernales earthquake (Fig. S17), raising the possibility that the fringes could represent postseismic deformation. However we do not see similar coastal fringes in the preceding 12-d ascending track interferogram, in which we would expect any postseismic signal to be larger in amplitude, given that it is closer in time to the earthquake. Our interpretation, then, is that the fringes we identify in the ascending coseismic interferogram are coseismic deformation from the Muisne event.

4.4 The 2016 Norsup, Vanuatu earthquake

On 2016 April 28, a $M_w 7.0$ earthquake struck near the village of Norsup, on Malekula Island, Malampa Province, Vanuatu. The event was felt across the Vanuatu archipelago, although there were no reports of major damage. The seismic catalogue location for the event, close to the island shore, and its reverse-faulting USGS W-phase moment tensor mechanism led to an initial local tsunami warning being issued, although no significant run-up was subsequently detected, perhaps a result of its estimated 25 km source depth limiting the vertical deformation of the seafloor.

Sentinel-1 data coverage for Malekula Island, and for Vanuatu in general, during the early phase of IW mode acquisitions is poor. Regular acquisitions did not occur over the island until October 2016, some 6 months after the earthquake, and the handful of SAR images that were available before the event were acquired in October 2015, approximately 6 months before the earthquake. As a result, the shortest duration interferometric pair that we could form that covered the island (ascending track 154) had a duration of 366 d. The processed interferogram (Fig. 7a; details in Table 1) shows almost complete decorrelation, except for some areas around the shore of the island, likely a consequence of most land areas on the island being covered with dense tropical vegetation. As a result, we cannot identify any deformation signal associated with the earthquake and classify it as a non-detection.

Despite our failure to detect this particular event with Sentinel-1 data, the question remains whether it would have been possible had there been data routinely collected at regular, short intervals around the time of the earthquake. Two conditions would need to be satisfied for this to be the case: (i) the earthquake would need to produce a detectable deformation signal and (ii) there would be sufficient interferometric correlation in the InSAR data from the region for that deformation signal to be detected.

To address the first of these points, we process additional interferograms for the area using data from the ALOS-2 satellite—a pair

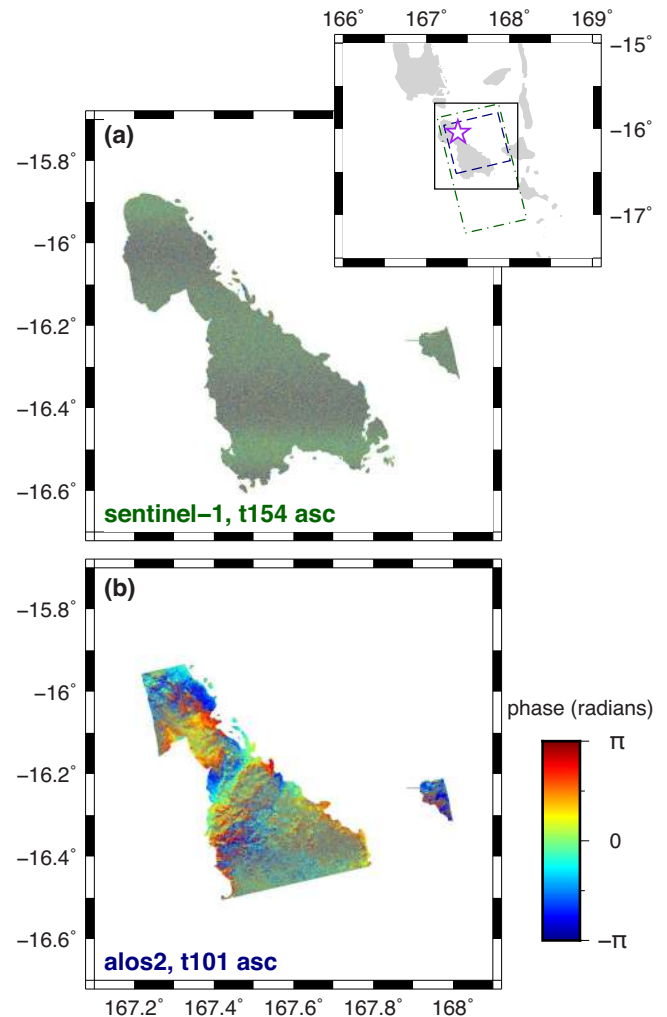


Figure 7. Interferograms spanning the 2016 Norsup earthquake. (a) Sentinel-1 interferogram (366-d time span), from ascending track 154. The interferogram is almost completely decorrelated, and the earthquake is not detected. (b) ALOS-2 interferogram (42-d time span), from track 018. There is a sufficient level of correlation in the interferogram to identify ~ 1.5 concentric fringes (~ 18 cm of range decrease), located close to the USGS epicentre (white star in inset), that could plausibly be the earthquake signal. Inset shows location of interferogram frames. [Green dot-dashes: Sentinel-1; blue dashes: ALOS-2.].

of ascending track stripmap images (ALOS-2 track 101) spanning 154 d—that we process using insarApp.py in ISCE as with the data from the Alor, Indonesia earthquake described above. The ALOS-2 interferogram (Fig. 7b; details in Table 2) shows 1.5 concentric fringes, consistent with approximately 18 cm of range decrease, immediately to the southwest of the USGS epicentre. The observed signal is consistent with the uplift expected from a moderate depth reverse-faulting earthquake under the island, as per the USGS source mechanism.

Next, in order to assess whether more rapid repeat coverage would be sufficient to avoid decorrelation in Vanuatu, we process a set of 12-d interferograms covering Malekula Island, from April to June 2017, a similar time of year to the 2016 earthquake. At present, 12-d repeat coverage is the shortest interval between acquisitions in the full Sentinel-1 IW archive over Vanuatu. These interferograms are plotted in Fig. S36. We find that the level of decorrelation in 12 d is severe, rendering the interferograms unusable for the purposes of

deformation study; all six have mean epicentral correlation values of ~ 0.35 , similar to the coseismic interferogram (see Section 5.1 below for more explanation). In the case of earthquake detection on Malekula Island, therefore, an even shorter repeat interval (i.e. 6 d) may be necessary to obtain a useable level of interferometric correlation.

5 DISCUSSION AND CONCLUSIONS

5.1 Factors affecting interferometric correlation and earthquake detectability with Sentinel-1 data

Our results show that the primary control on earthquake detectability is interferometric correlation—without coherent (well-correlated) interferograms it is not possible to identify the signal produced by earthquakes. As we discuss above, there are multiple factors that can cause reductions in correlation, the most important being spatial effects (related to perpendicular baseline), and volume and temporal effects (related to vegetation density and interferogram time span). Here we make use of our estimates of mean epicentral correlation for each event interferogram (Table 1) and explore the relationships between these and interferogram time span, perpendicular baseline and latitude, broken down by earthquake magnitude, in Fig. 8.

We find that the detectability of earthquakes at a given level of correlation, is strongly magnitude dependent. Of the seven events with $M_w \geq 7$, six were from interferograms with mean epicentral correlation less than 0.4, and of those, five were detected. (The lone undetected $M_w \geq 7$ event, the 2016 Norsup, Vanuatu earthquake, described in Section 4.4, had the longest time span—1 yr—and likely was subject to severe temporal decorrelation.) In comparison, of the events in the range M_w 5.5–6.0, none of the six interferograms with mean epicentral correlation of 0.4 or lower resulted in a successful event detection, five being non-detections, and one ambiguous. The events of intermediate size, with M_w 6–7 and mean epicentral correlation < 0.4 , were split between non-detections (five events) and detections/ambiguous interferograms (three events).

We suggest two reasons for these differences in event detectability at different magnitudes and correlation levels: First, larger earthquakes produce deformation with a larger spatial extent – i.e. displacement that is manifest over a larger area – than smaller events; coherent deformation signals over large areas are easier to identify than those over small areas, and are less likely to be obscured or hidden by areas of very high decorrelation, especially in the far-field (i.e. distances > 20 km from the causative fault). Second, larger earthquakes can cause decorrelation in the near-field (i.e. within 20 km of the fault) of an earthquake that would act to reduce the mean epicentral correlation. For instance, larger earthquakes are more likely to rupture the surface, and cause secondary effects like building damage, liquefaction, and landsliding, all of which can increase the amount of decorrelation in an area; indeed decorrelation in coseismic interferograms can be used as a proxy for building damage in urban areas (e.g. Fielding *et al.* 2005; Yun *et al.* 2015). In addition, as in the cases of the M_w 7.8 Gorkha and Kaikoura earthquakes (Figs S1 and S33, respectively), the large displacements of the ground that can be produced by large earthquakes can themselves be responsible for decorrelation. If surface displacements are a significant fraction of, or larger than, the pixel size, they can cause localized differences in illumination, and therefore changes in the reflectivity spectrum, and decorrelation. Thus, that

large earthquakes can be detected and also have low mean epicentral correlations, may reflect a trade-off between potential increases in the areal coverage of detectable signal and the potential decorrelation caused by the surface deformation, damage and secondary effects that those large earthquakes can cause.

In terms of the factors controlling interferometric correlation in our data set, we find that the highest mean epicentral correlations (0.5 and higher) were from interferograms with short time spans (24 d or less), and short perpendicular baselines (50 m or less), as might be expected. However, these ‘optimal’ combinations of short time spans and baselines do not predict high interferometric correlation, or indeed successful detections, alone. Out of the 16 earthquakes where such short time span, short perpendicular baseline interferograms could be produced, only nine had mean epicentral correlations of 0.4 or greater, resulting in eight detections. The remaining seven events with mean epicentral correlations of less than 0.4 included four non-detections. It is apparent, therefore, that baseline and time span alone do not control correlation and earthquake detectability.

One factor to consider is latitude, which we propose is a proxy for vegetation density, and is the strongest predictor of decorrelation in our event interferograms. Of the six undetected events with optimal baselines and time spans, five occurred within the latitude band between 15°N and 15°S . This latitude band includes much of the intertropical convergence zone (ICTZ), a feature of the atmospheric Hadley circulation marked by a global belt of clouds and a corresponding time-mean peak in latitudinal precipitation (e.g. Philander *et al.* 1995). These climate conditions are correlative with a belt of dense tropical vegetation on the ground in Central America, northern South America, sub-Saharan Africa and Southeast Asia. Considering all of the 11 events that occurred in this latitude range, none of the interferograms had mean epicentral correlation greater than 0.38, seven events were not detected, and two produced ambiguous interferograms. If, as we suspect, the tropical vegetation associated with the ICTZ is the cause of low interferometric correlation and poor earthquake detectability, it may be necessary to modify the Sentinel-1 mission strategy to acquire data in these regions with the shortest possible recurrence interval, i.e. every 6 d, in order to mitigate the temporal decorrelation and volume scattering effects of such vegetation.

5.2 The role of atmospheric noise in earthquake detectability

So far we have not dwelled on the implications of atmospheric noise in our search for earthquake detections. In our classification, earthquakes for which we produce interferograms that are sufficiently well-correlated but affected by atmospheric noise are categorized as ‘ambiguous’. Typically, these are interferograms in which there are multiple features that have the approximate dimensions (e.g. between 5 km and 20 km) and amplitudes (e.g. up to 3 fringes) that might be expected for the deformation signal of an earthquake. The source of these features is typically water vapour in the troposphere, specifically the turbulent portion of the troposphere. Unlike the ‘static’ portion of the troposphere, related to the capacity of the air in the troposphere to sustain water vapour, that can be estimated from meteorological data (i.e. surface temperature, pressure and relative humidity) or weather models, and is modulated by the topography, it is not currently possible to estimate the turbulent troposphere component without additional information. For example, if there is a network of continuous GPS stations within a SAR scene,

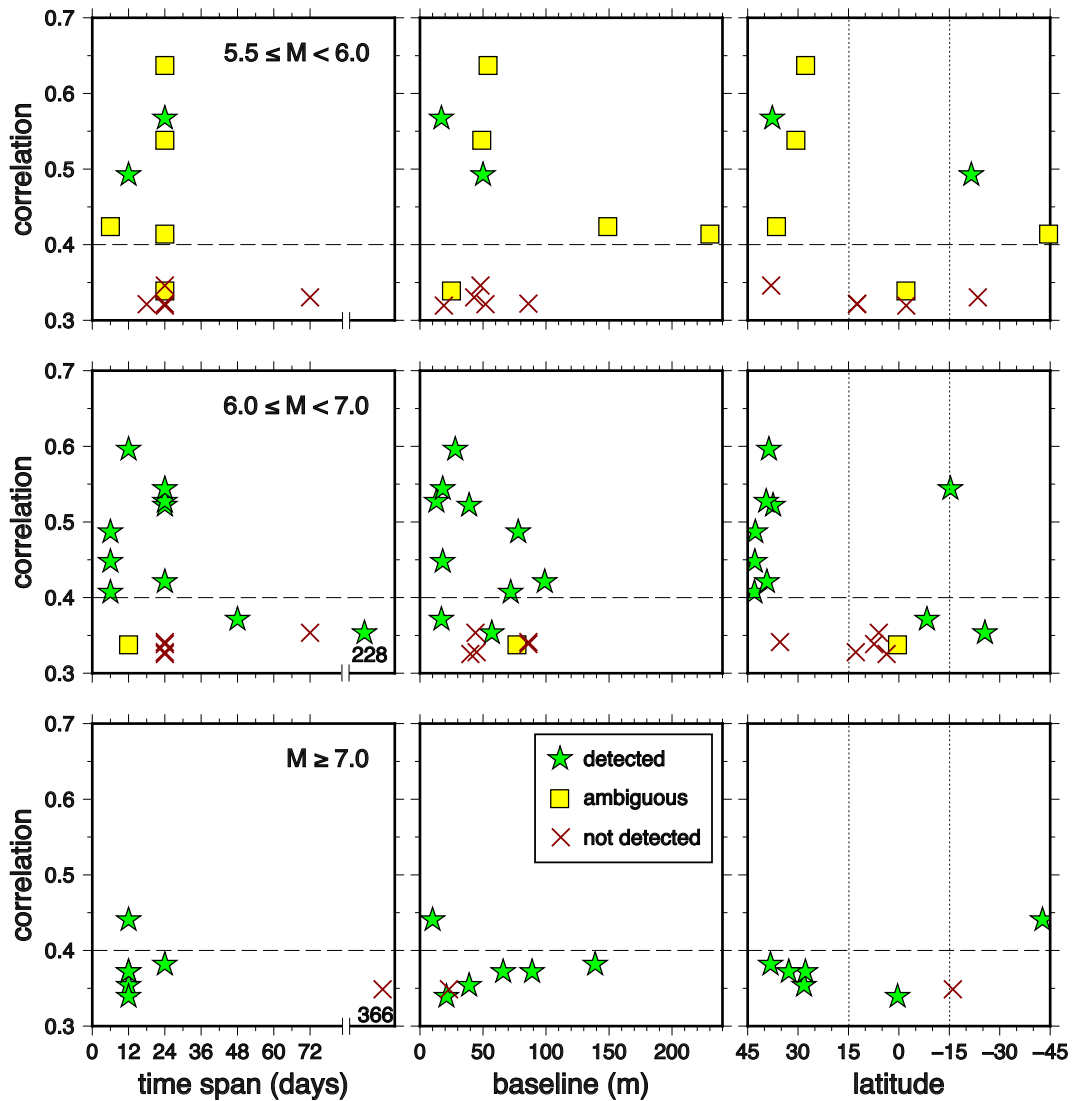


Figure 8. Exploration of factors affecting correlation and earthquake detectability in the 35 Sentinel-1 coseismic interferograms considered in this study. We divide the events into three categories by moment: $5.5 \leq M < 6.0$ (top row), $6.0 \leq M < 7.0$ (middle row), $M \geq 7.0$ (bottom row), and consider the relationship between mean epicentral correlation and interferogram time span (left column), perpendicular baseline (central column) and latitude (right column). The interferograms with the highest correlations (0.5 and higher) tend to have time spans of 24 d or less and baselines of 50 m or less. The interferograms with the lowest correlation (0.35 or less) are mostly at low latitudes (between -15° and 15°), regardless of baseline or time span. Detectability strongly depends on magnitude, with a majority of $M \geq 6.0$ events being detected, and on latitude, with most high latitude events (greater than 15° from the equator) being detected. All non-detected events have correlation less than 0.4 (a majority 0.35 or less), but most $M \geq 7.0$ events are still detectable in those conditions. [Green stars: detected events; yellow squares: events with ambiguous interferograms; red crosses: non-detected events.].

it is possible to use zenith delays estimated at each station at each SAR acquisition time during GPS processing to estimate a line-of-sight correction for interferograms (e.g. Li *et al.* 2006; Houlié *et al.* 2016). Alternatively, several studies have demonstrated the value of time-series processing for the identification and removal of spatially-correlated atmospheric noise within coseismic interferograms, most notably in the recent case of the 2017 Pawnee, Oklahoma earthquake in the central United States (e.g. Grandin *et al.* 2017; Fielding *et al.* 2017), where it is not possible to identify the earthquake deformation otherwise. (We classify the interferogram for the Pawnee event, plotted in Fig. S25, as ambiguous, being dominated by a nine-fringe atmospheric gradient that overwhelms any earthquake signal present.)

Overall, of the six earthquakes whose interferograms we classify as ambiguous, five of the events are overprinted and/or obscured

by atmospheric noise. It is possible that with additional information or analysis, that some of these earthquakes could become detected events with Sentinel-1 data; however with a single interferogram this is not, in our opinion, possible.

Finally, we consider whether the significant levels of atmospheric noise seen in some cases (e.g. Figs S2, S15, S19) can be attributed to the design of the Sentinel-1 mission. Qualitatively, compared with past C-band missions such as ERS and Envisat, we identify higher levels of spatially correlated noise in these interferograms, in particular signals that mimic the topography. We suspect that this can be attributed to two factors. First, the Sentinel-1 IW mode spans a shallower range of radar incidences – between 30° and 45° – compared with the 17° to 27° range used by earlier missions (ERS and the default IM2 mode of Envisat). As a consequence, we would expect the two-way path of the radar through the troposphere to

be longer for the Sentinel-1 satellites in IW mode, and thus they will be more strongly affected by path delays. Second, the shorter average time spans between acquisitions and tighter orbital control of the Sentinel-1 mission, coupled with its shallower incidence in IW mode, lead to improved correlation in areas of steep topography compared with earlier missions. These are the areas in which differences in static troposphere delay will be most accentuated in interferograms – in other words, this could be considered a measure of the success of the mission at improving the overall coherence of interferograms! In the case of the smaller earthquakes that can be obscured by this tropospheric noise, however, we should still recognize the need to develop methods to mitigate such noise in near-real time if Sentinel-1 data are to be used operationally to monitor earthquakes.

5.3 The magnitude of completeness for shallow earthquakes studied with Sentinel-1

Our efforts to examine earthquake detectability with Sentinel-1 IW data, perhaps unsurprisingly have shown that proportionately more ‘large’ ($M_w \geq 7.0$) and ‘moderate’ ($6.0 \leq M_w < 7.0$) earthquakes were detected than small events ($5.5 \leq M_w < 6.0$). With this in mind, we attempt to estimate here a ‘magnitude of completeness’ – a quantity estimated for instrumental seismic catalogues that describes the smallest event size that is always captured in a given catalogue – for earthquakes studied using Sentinel-1 IW data, a guide as to whether an event of a given size in a given hypocentral depth range would be expected to be detectable in any conditions. We retain our hypocentral depth range bounds for each magnitude range, in order to restrict the consideration to events that ought to be detectable – i.e. those that could produce a detectable deformation signal.

At present, the largest earthquake that we have not detected is the $M_w 7.0$ Norsup, Vanuatu event, which produced a deformation signal that was detectable using ALOS-2 (Section 4.4). However, the Sentinel-1 interferogram for the Norsup event had the longest time span – 1 yr – of any interferogram in our study, so it is perhaps not a safe event from which to draw generalizations. (It is also by no means certain, of course, that the current, shorter, 12-d time span would have resulted in detection, given the level of decorrelation shown in our tests; Fig. S36.) We might also consider the $M_w 6.2$ Kurayoshi, Japan earthquake as a relevant event for our estimate. While the event was successfully detected in the ascending track interferogram (Fig. 5b), it was not detected in the descending track interferogram (Fig. 5a), which had the earlier of the two post-event acquisitions, due to decorrelation. In the case of Kurayoshi, the inability to detect with one 24-d interferogram an event that was detectable in another 24-d interferogram, might suggest an event that is close to the detection threshold.

We suggest that the Norsup and Kurayoshi events could be considered upper ($M_w 7.0$) and lower ($M_w 6.2$) bounds on the magnitude of completeness for global earthquakes studied using Sentinel-1 data. We anticipate that over the coming years of the Sentinel-1 mission, more systematic studies of earthquake detectability will help to reduce the range of estimates. In order to lower this magnitude to $M_w 6.0$ or below, given the discussion on detectability above, we suggest that more frequent acquisitions will likely be necessary in low latitude areas, to combat the effects of decorrelation in Sentinel-1 IW interferograms.

ACKNOWLEDGEMENTS

Sentinel-1 InSAR data are copyrighted by the European Space Agency, and are additionally distributed by the Alaska Satellite Facility. ALOS-2 InSAR data are copyrighted by the Japanese Aerospace Exploration Agency, and were made available under RA-4 project 1356. We are grateful to the Associate Editor and two anonymous reviewers whose comments and feedback have helped to improve the manuscript. Ruth Amey is thanked for useful discussions about the Kurayoshi earthquake. A.G. acknowledges support from the GEODE project, funded by NSF Award 1600314, and assistance from Rosemarie Bisquera, Mary Droser and Bill Phelps. We use the GMT software (Wessel *et al.* 2013) to produce our figures.

REFERENCES

- Bürgmann, R., Rosen, P. & Fielding, E., 2000. Synthetic Aperture Radar interferometry to measure Earth's surface topography and its deformation, *Ann. Rev. Earth. planet. Sci.*, **28**, 169–209.
- Chen, C.W. & Zebker, H.A., 2002. Phase unwrapping for large SAR interferograms: Statistical segmentation and generalized network models, *IEEE Trans. Geosci. Remote Sens.*, **40**, 1709–1719.
- De Zan, F. & Guarnieri, A.M., 2006. TOPSAR: Terrain Observation by Progressive Scans, *IEEE Trans. Geosci. Remote Sens.*, **44**, 2352–2360.
- DeLong, S.B. *et al.*, 2016. Tearing the terror: details and implications of surface rupture and deformation from the 24 August 2014 M6.0 South Napa earthquake, California, *Earth Space Sci.*, **3**, 416–430.
- Elliott, J.R., Walters, R.J. & Wright, T.J., 2016. The role of space-based observation in understanding and responding to active tectonics and earthquakes, *Nat. Comms.*, **7**(13844), doi:10.1038/ncomms13844.
- Farr, T.G. *et al.*, 2007. The Shuttle Radar Topography Mission, *Rev. Geophys.*, **45**(RG2004), doi:10.1029/2005RG000183.
- Ferreira, A.M.G., Weston, J. & Funning, G.J., 2011. Global compilation of interferometric synthetic aperture radar earthquake source models: 2. Effects of 3-D Earth structure, *J. geophys. Res.*, **116**(B08409), doi:10.1029/2010JB008132.
- Fielding, E.J., Wright, T.J., Muller, J., Parsons, B. & Walker, R., 2004. Aseismic deformation of a fold-and-thrust belt imaged by SAR interferometry near Shahdad, SE Iran, *Geology*, **32**, 577–580.
- Fielding, E.J., Talebian, M., Rosen, P.A., Nazari, H., Jackson, J.A., Ghosh, M. & Walker, R., 2005. Surface ruptures and building damage of the 2003 Bam, Iran earthquake mapped by satellite SAR interferometric correlation, *J. geophys. Res.*, **110**(B03302), doi:10.1029/2004JB003299.
- Fielding, E.J., Sangha, S.S., Bekaert, D.P.S., Samsonov, S.V. & Chang, J.C., 2017. Surface deformation of north-central Oklahoma related to the 2016 M_w 5.8 Pawnee earthquake from SAR interferometry time series, *Seismol. Res. Lett.*, **110**(4), 12.
- Floyd, M.A. *et al.*, 2016. Spatial variations in fault friction related to lithology from rupture and afterslip of the 2014 South Napa, California, earthquake, *Geophys. Res. Lett.*, **43**, 6808–6816.
- Funning, G.J., 2005. Source parameters of large shallow earthquakes in the Alpine-Himalayan belt from InSAR and waveform modelling, *D.Phil. thesis*. University of Oxford, Oxford, UK.
- Funning, G.J., Parsons, B., Wright, T.J., Jackson, J.A. & Fielding, E.J., 2005. Surface displacements and source parameters of the 2003 Bam (Iran) earthquake from Envisat advanced synthetic aperture radar imagery, *J. geophys. Res.*, **110**(B09406), .
- Goldstein, R.M. & Werner, C.L., 1998. Radar interferogram filtering for geophysical applications, *Geophys. Res. Lett.*, **25**(21), 4035–4038.
- Gomba, G., Parizzi, A., Zan, F.D., Eineder, M. & Bamler, R., 2016. Toward operational compensation of ionospheric effects in SAR interferograms: the split-spectrum method, *IEEE Trans. Geosci. Remote Sens.*, **54**(3), 1446–1460.
- Gonzalez-Garcia, J.J. *et al.*, 2010. *Seismotectonics of the 2010 El Mayor Cucapah - Indiviso earthquake and its relation to seismic hazard in southern*

- California, Abstract T53B-2117 presented at 2010 Fall Meeting. AGU, San Francisco, CA. p. 13.
- Grandin, R., Klein, E., Métois, M. & Vigny, C., 2016. Three-dimensional displacement field of the 2015 M_w 8.3 Illapel earthquake (Chile) from across- and along-track Sentinel-1 TOPS interferometry, *Geophys. Res. Lett.*, **43**, 2552–2561.
- Grandin, R., Vallée, M. & Lacassin, R., 2017. Rupture process of the M_w 5.8 Pawnee, Oklahoma, earthquake from Sentinel-1 InSAR and seismological data, *Seismol. Res. Lett.*, **88**, 11.
- Gurrola, E.M., Agram, P.S., Laval, M., Sacco, G.F. & Rosen, P.A., 2016. *The InSAR Scientific Computing Environment (ISCE): An Earth science SAR processing framework, toolbox, and foundry*, Abstract G43A-1039 presented at 2016 Fall Meeting. AGU, San Francisco, CA. p. 12.
- Houlié, N., Funning, G.J. & Bürgmann, R., 2016. Use of a GPS-derived troposphere model to improve InSAR deformation estimates in the San Gabriel Valley, California, *IEEE Trans. Geosci. Remote Sens.*, **54**, 5365–5374.
- Jolivet, R., Grandin, R., Lesserre, C., Doin, M.-P. & Peltzer, G., 2011. Systematic InSAR tropospheric phase delay corrections from global meteorological reanalysis data, *Geophys. Res. Lett.*, **38**, doi:10.1029/2011GL048757.
- Li, Z., Fielding, E.J., Cross, P. & Muller, J.P., 2006. Interferometric synthetic aperture radar atmospheric correction: GPS topography-dependent turbulence model, *J. geophys. Res.*, **111**(B02404), doi:10.1029/2005JB003711.
- Li, Z., Pasquali, P., Cantone, A., Singleton, A., Funning, G. & Forrest, D., 2012. MERIS atmospheric water vapor correction model for wide swath interferometric synthetic aperture radar, *IEEE Geosci. Remote Sens. Lett.*, **9**, 257–261.
- Lohman, R.B. & Simons, M., 2005. Locations of selected small earthquakes in the Zagros mountains, *Geochem. Geophys. Geosys.*, **6**(3), Q03001.
- Massonnet, D. & Feigl, K.L., 1998. Radar interferometry and its application to changes in the earth's surface, *Rev. Geophys.*, **36**(4), 441–500.
- Massonnet, D., Rossi, M., Carmona, C., Adragna, F., Peltzer, G., Feigl, K. & Rabaute, T., 1993. The displacement field of the Landers earthquake mapped by radar interferometry, *Nature*, **364**, 138–142.
- Mellors, R.J., Magistrale, H., Earle, P. & Cogbill, A., 2004. Comparison of four moderate-size earthquakes in southern California using Seismology and InSAR, *Bull. seism. Soc. Am.*, **94**(6), 2004–2014.
- Moore, R.K., Claassen, J.P. & Lin, Y.H., 1981. Scanning spaceborne synthetic aperture radar with integrated radiometer, *IEEE Trans. Aerosp. Electron. Syst.*, **17**, 410–420.
- Nissen, E., Elliott, J.R., Sloan, R.A., Craig, T.J., Funning, G.J., Hutko, A., Parsons, B.E. & Wright, T.J., 2016. Limitations of rupture forecasting exposed by instantaneously triggered earthquake doublet, *Nat. Geosci.*, **9**, 330–336.
- Okada, Y., 1985. Surface deformation due to shear and tensile faults in a half-space, *Bull. seism. Soc. Am.*, **75**(4), 1135–1154.
- Philander, S.G.H., Gu, D., Halpern, D., Lambert, G., Lau, N.-C., Li, T. & Pacanowski, R.C., 1995. Why the ICTZ is mostly north of the equator, *J. Climate*, **9**, 2958–2972.
- Rosen, P.A., Hensley, S., Joughin, I.R., Li, F.K., Madsen, S.N., Rodriguez, E. & Goldstein, R.M., 2000. Synthetic aperture radar interferometry, *Proc. IEEE*, **88**(3), 333–382.
- Rosen, P.A., Gurrola, E.M., Sacco, G. & Zebker, H., 2011. *InSAR Scientific Computing Environment (ISCE) – the home stretch*, Abstract IN42A-02 presented at 2011 Fall Meeting. AGU, San Francisco, CA. p. 5.
- Rosich, B., Grimon, P., Sabella, G., Zito, F.L., Izzo, G.P., Miranda, N., Potin, P. & Monjoux, E., 2017. *Sentinel-1 Mission Operations status, Fringe 2017*, Helsinki, Finland.
- Salvi, S., Stramondo, S., Funning, G.J., Ferretti, A., Sarti, F. & Mouratidis, A., 2012. The Sentinel-1 mission for the improvement of the scientific understanding and the operational monitoring of the seismic cycle, *Remote Sens. Environ.*, **120**, 164–174.
- Scholz, C., 2002. *The Mechanics of Earthquakes and Faulting*, 2nd edn, Cambridge University Press.
- Talebian, M. *et al.*, 2004. The 2003 bam (Iran) earthquake: rupture of a blind strike-slip fault, *Geophys. Res. Lett.*, **31**, L11611.
- Torres, R. *et al.*, 2012. GMES Sentinel-1 mission, *Remote Sens. Environ.*, **120**, 9–24.
- Weber Hoen, E. & Zebker, H.A., 2000. Penetration depths inferred from interferometric volume decorrelation observed over the Greenland Ice Sheet, *IEEE Trans. Geosci. Remote Sens.*, **38**, 2571–2583.
- Wei, M. & Sandwell, D.T., 2010. Decorrelation of L-band and C-band interferometry over vegetated areas in California, *IEEE Trans. Geosci. Remote Sens.*, **48**(7), 2942–2952.
- Wesnousky, S.G., Scholz, C.H. & Shimazaki, K., 1982. Deformation of an island arc: Rates of moment release and crustal shortening in intraplate Japan determined from seismicity and Quaternary fault data, *J. geophys. Res.*, **87**(B8), 12 587–12 631.
- Wessel, P., Smith, W. H.F., Scharroo, R., Luis, J.F. & Wobbe, F., 2013. Generic Mapping Tools: Improved version released, *EOS, Trans. Am. geophys. Un.*, **94**, 409–410.
- Weston, J., Ferreira, A.M.G. & Funning, G.J., 2011. Global compilation of interferometric synthetic aperture radar earthquake source models: 1. Comparisons with seismic catalogs, *J. geophys. Res.*, **116**(B08408), doi:10.1029/2010JB008131.
- Weston, J., Ferreira, A. M.G. & Funning, G.J., 2012. Systematic comparisons of earthquake source models determined using InSAR and seismic data, *Tectonophysics*, **532**, 61–81.
- Yun, S.-H. *et al.*, 2015. Rapid damage mapping for the 2015 M_w 7.8 Gorkha earthquake using synthetic aperture radar data from COSMO-SkyMed and ALOS-2 satellites, *Seismol. Res. Lett.*, **86**, 1549–1551.
- Zebker, H.A. & Villasenor, J., 1992. Decorrelation in interferometric radar echoes, *IEEE Trans. Geosci. Remote Sens.*, **30**(5), 950–959.

SUPPORTING INFORMATION

Supplementary data are available at [GJI](https://doi.org/10.1002/gji.12914) online.

Figure S1. Coseismic interferogram for the 25 April 2015 Gorkha, Nepal earthquake. This is classified as a detected event; the eastern half of the interferogram shows concentric deformation fringes. Pink star indicates USGS epicentre for the event, pink box indicates area used to calculate average interferometric correlation. Interferogram is overlaid upon a 30 m resolution SRTM DEM (Farr *et al.*, 2007). Details of the interferogram are given in Table 1.

Figure S2. Coseismic interferogram for the 2015 May 4 Wanaka, New Zealand earthquake. This is classified as ambiguous; while there is a good level of interferometric correlation, it is not clear which features are earthquake deformation and which are atmospheric noise. Other details as for Fig. S1.

Figure S3. Coseismic interferogram for the 2015 May 12 Kodari, Nepal earthquake. This is classified as a detected event; concentric deformation fringes can be seen in the centre of the interferogram. Other details as for Fig. S1.

Figure S4. Coseismic interferogram for the 2015 June 4 Ranau, Malaysia earthquake. This event is classified as not detected; decorrelation obscures any earthquake features. Other details as for Fig. S1.

Figure S5. Coseismic interferogram for the 2015 July 3 Pishan, China earthquake. This event is classified as detected; concentric deformation fringes can be seen in the west of the interferogram. Other details as for Fig. S1.

Figure S6. Coseismic interferogram for the 2015 August 7 Lake Kivu, Democratic Republic of Congo earthquake. This is classified as ambiguous; fringes can be identified on the shores of the lake, but it is not clear if any of them represent the earthquake. Other details as for Fig. S1.

Figure S7. Coseismic interferogram for the 2015 October 23 Abepura, Indonesia earthquake. This event is classified as not detected; decorrelation obscures any earthquake signal. Other details as for Fig. S1.

Figure S8. Coseismic interferogram for the 2015 November 4 Alor, Indonesia earthquake. This is classified as a detected event; the eastern portion of the interferogram contains fringes consistent with an earthquake (see section 4.1 for more details). Other details as for Fig. S1.

Figure S9. Coseismic interferogram for the 2015 November 17 Lefkada, Greece earthquake. This is classified as a detected event; despite the land masses being a series of discontinuous islands, coherent, continuous fringes can be identified between them. Other details as for Fig. S1.

Figure S10. Coseismic interferogram for the 2015 November 29 Yuto, Argentina earthquake. This event is classified as not detected; decorrelation obscures any earthquake signal. Other details as for Fig. S1.

Figure S11. Coseismic interferogram for the 2015 December 7 Murghob, Tajikistan earthquake. This is classified as a detected event; diagonal concentric bands of deformation fringes can be identified across the centre of the interferogram. Other details as for Fig. S1.

Figure S12. Coseismic interferogram for the 2015 December 20 Tarakan, Indonesia earthquake. This event is classified as not detected; decorrelation obscures any earthquake signal. Other details as for Fig. S1.

Figure S13. Coseismic interferogram for the 2016 January 20 Hongtu, China earthquake. This is classified as a detected event; two concentric deformation fringes can be identified in the west of the interferogram. Other details as for Fig. S1.

Figure S14. Coseismic interferogram for the 2016 March 18 Vanj, Tajikistan earthquake. This event is classified as not detected; decorrelation obscures any earthquake signal. Other details as for Fig. S1.

Figure S15. Coseismic interferogram for the 2016 March 21 Khuzdar, Pakistan earthquake. This is classified as ambiguous; there is a good level of interferometric correlation and fringes can be identified throughout, but it is not clear if any of them represent the earthquake. Other details as for Fig. S1.

Figure S16. Coseismic interferogram for the 2016 April 15 Kumamoto, Japan earthquake. This is classified as a detected event; concentric deformation fringes extend diagonally across the south-west of the interferogram. Other details as for Fig. S1.

Figure S17. Coseismic interferogram for the 2016 April 16 Pedernales, Ecuador earthquake. This is classified as a detected event; despite a low level of interferometric correlation, continuous, concentric deformation fringes extend across the southern half of the interferogram. Other details as for Fig. S1.

Figure S18. Coseismic interferogram for the 28 April 2016 Norsup, Vanuatu earthquake. This event is classified as not detected; decorrelation obscures any earthquake signal (see section 4.4 for more details). Other details as for Fig. S1.

Figure S19. Coseismic interferogram for the 2016 May 13 Qila Abdullah, Pakistan earthquake. This is classified as ambiguous; there is a good level of interferometric correlation and fringes can be identified throughout, but it is not clear if any of them represent the earthquake. Other details as for Fig. S1.

Figure S20. Coseismic interferogram for the 2016 May 18 Muisine, Ecuador earthquake, from descending track 040. This is classified as ambiguous. Other details as for Fig. S1.

Figure S21. Coseismic interferogram for the 2016 May 16 Petermann Ranges, Australia earthquake. This is classified as a detected

event; concentric deformation fringes can be identified in the centre of the interferogram. Other details as for Fig. S1.

Figure S22. Coseismic interferogram for the 2016 June 10 Puerto Morazan, Nicaragua earthquake. This event is classified as not detected; decorrelation obscures any earthquake signal. Other details as for Fig. S1.

Figure S23. Coseismic interferogram for the 2016 June 26 Sary-Tash, Kyrgyzstan earthquake. This is classified as a detected event; concentric deformation fringes can be identified in the centre of the interferogram. Other details as for Fig. S1.

Figure S24. Coseismic interferogram for the 2016 August 24 Amatrice, Italy earthquake. This is classified as a detected event; concentric deformation fringes can be identified in the southern portion of the interferogram. Other details as for Fig. S1.

Figure S25. Coseismic interferogram for the 2016 September 3 Pawnee, Oklahoma, USA earthquake. This is classified as ambiguous. Other details as for Fig. S1.

Figure S26. Coseismic interferogram for the 2016 September 14 Mutata, Colombia earthquake. This event is classified as not detected; decorrelation obscures any earthquake signal. Other details as for Fig. S1.

Figure S27. Coseismic interferogram for the 2016 September 15 La Paz Centro, Nicaragua earthquake. This is classified as not detected. Other details as for Fig. S1.

Figure S28. Coseismic interferogram for the 2016 September 22 Machaze, Mozambique earthquake. This is classified as a detected event; concentric deformation fringes can be identified in the north-west portion of the interferogram. Other details as for Fig. S1.

Figure S29. Coseismic interferogram for the 2016 September 28 Nagarote, Nicaragua earthquake. This event is classified as not detected; decorrelation obscures any earthquake signal. Other details as for Fig. S1.

Figure S30. Coseismic interferogram for the 2016 October 21 Ku-rayoshi, Japan earthquake, from descending track 090. It is not possible to detect the earthquake from this interferogram; decorrelation obscures any earthquake signal (see Section 4.2 for details). Other details as for Fig. S1.

Figure S31. Coseismic interferogram for the 26 October 2016 Visso, Italy earthquake. This is classified as a detected event; concentric deformation fringes can be identified in the southern portion of the interferogram. Other details as for Fig. S1.

Figure S32. Coseismic interferogram for the 2016 October 30 Norcia, Italy earthquake. This is classified as a detected event; concentric deformation fringes can be identified in the southern portion of the interferogram. Other details as for Fig. S1.

Figure S33. Coseismic interferogram for the 2016 November 13 Kaikoura, New Zealand earthquake. This is classified as a detected event; concentric deformation fringes can be identified aligned parallel to the coast. Other details as for Fig. S1.

Figure S34. Coseismic interferogram for the 2016 November 25 Akto, China earthquake. This is classified as a detected event; a four-quadrant deformation pattern indicates the earthquake. Other details as for Fig. S1.

Figure S35. Coseismic interferogram for the 2016 December 1 Huarichancara, Peru earthquake. This is classified as a detected event; concentric deformation fringes in the centre of the interferogram indicate the earthquake. Other details as for Fig. S1.

Figure S36. 12-Day interferograms of Melampa Island, Vanuatu, the epicentral region of the 2016 Norsup, Vanuatu earthquake. Each interferogram is labelled with its acquisition dates, perpendicular baseline (bperp) and mean epicentral correlation (corr). All interferograms are noisy, have low mean epicentral correlation, and would

be unlikely to record earthquake deformation, suggesting that a 12-d repeat interval is insufficient for successful earthquake studies in this region.

Figure S37. Detectability of events as a function of baseline and time span, for events that occurred in the mid-latitudes [$\pm(15^\circ$ to $45^\circ)$, left column], and in the low latitudes, [-15° to 15° , right column]. Events are further subdivided into different magnitude ranges (top three rows), and all magnitudes (bottom row). The mid-latitudes have a far higher proportion of successful detections than the low latitudes. The majority of successful detections for the mid-latitude events appear to cluster in the lower left of the plot (i.e. time

span 24 d or less, baseline <50 m) at all magnitudes. These same conditions do not result in a majority of successful detections in the low latitudes, where there are proportionately more non-detections. [Green stars: detections. Yellow squares: ambiguous. Red crosses: non-detections.]

Please note: Oxford University Press is not responsible for the content or functionality of any supporting materials supplied by the authors. Any queries (other than missing material) should be directed to the corresponding author for the article.